Neutrino portals, terrestrial upscattering, and atmospheric neutrinos

R. Andrew Gustafson,[1,*] Ryan Plestid,[2,3,†] and Ian M. Shoemaker[1,‡]
[1]*Department of Physics, Center for Neutrino Physics, Virginia Tech University, Blacksburg, Virginia 24061, USA*
[2]*Department of Physics and Astronomy, University of Kentucky, Lexington, Kentucky 40506, USA*
[3]*Theoretical Physics Department, Fermilab, Batavia, Illinois 60510, USA*

(Received 16 August 2022; accepted 7 November 2022; published 29 November 2022)

We consider the upscattering of atmospheric neutrinos in the interior of Earth producing heavy neutral leptons (HNLs) which subsequently decay inside large volume detectors (e.g., Super-Kamiokande or DUNE). We compute the flux of upscattered HNLs arriving at a detector and the resultant event rate of visible decay products. Using Super-Kamiokande's atmospheric neutrino dataset we find new leading constraints for dipole couplings to any flavor with HNL masses between roughly 10 and 100 MeV. For mass mixing with tau neutrinos, we probe new parameter space near HNL masses of ∼20 MeV with prospects for substantial future improvements. We also discuss prospects at future experiments such as DUNE, JUNO, and Hyper-Kamiokande.

DOI: 10.1103/PhysRevD.106.095037

I. INTRODUCTION

Heavy neutral leptons (HNLs) are well motivated extensions of the Standard Model (SM). They appear ubiquitously in dark sector models and are especially important because their coupling to neutrinos represents one of three unique renormalizable "portals" between a generic dark sector and the Standard Model [1–4]. They are natural partners to left-handed neutrinos, reflecting a matching of chiral degrees of freedom observed among all other SM fermions, and their nonobservation is easily explained due to their being a SM gauge singlet. They are further motivated by anomaly cancellation arguments that become essential in models with new gauge groups, e.g., a gauged $B-L$ [5,6]. HNLs appear as necessary ingredients in certain grand unified theories, e.g., SO(10) [7], and they are intimately connected to neutrino masses.[1]

Despite their strong theoretical motivation, there is no model-independent prediction for the HNL mass scale. HNLs may be $O(\mathrm{eV})$ in mass (i.e., sterile neutrinos) and connected to neutrino masses via a naive Dirac mass mechanism (like all other SM fermions), in which case they are most easily searched for using short-baseline oscillation experiments or cosmological observables. Alternatively, neutrino masses may be generated by a type-I [11–13] seesaw mechanism each of which leads to different expected mass scales for different Yukawa couplings.

The ubiquity of HNLs in generic models of a dark sector and their unconstrained mass range therefore motivates a broad search strategy that targets many decades of HNL mass parameter space, ranging from the eV to the GeV (or even TeV) scale [14–27]. In this work we will demonstrate that large volume detectors can efficiently search for HNLs via their decays by leveraging atmospheric neutrino upscattering inside Earth. This search strategy is ideally suited to HNL decay lengths λ, satisfying $10\ \mathrm{m} \lesssim \lambda \lesssim 6000\ \mathrm{km}$ with the upper limit set by Earth's radius. This complements fixed target "beam dump" experiments and missing energy searches which typically lose sensitivity as the HNL decay length becomes much longer than the experimental apparatus, which tend to range from 10's to 100's of meters (much shorter than the 1000's of kilometers that characterize Earth's radius). We derive new and leading constraints for HNL masses between ∼10 and 200 MeV, a mass range which has interesting implications for models that address the Hubble tension [28].

Much of the literature on HNLs focuses on the aforementioned renormalizable coupling between HNLs and active neutrinos available in the SM. This is the so-called mass-mixing portal, which results in a small admixture of HNL contamination among the active neutrinos

*gustafr@vt.edu
†rpl225@uky.edu
‡shoemaker@vt.edu

[1]The Zee-Babu mechanism [8–10] is a notable counterexample in which neutrino masses are induced via new scalars rather than fermions.

$$\nu_\alpha = U_{\alpha N} N + \sum_{i=1}^{3} U_{\alpha i} \nu_i, \tag{1}$$

where U is the mixing angle, and where $\alpha \in \{e, \mu, \tau\}$ labels the active neutrino species in the flavor basis. This then induces a transition matrix element within the weak current, e.g., $\mathcal{L}_{\rm int} \supset U_{\alpha N} \bar{N}_i \gamma_\mu P_L \nu_\alpha J^\mu$.

Above the weak scale the mass-mixing portal is relevant in the Wilsonian sense, however, below the weak scale the mixing angle accompanies an irrelevant dimension-6 operator in the 4-Fermi effective theory that governs low-energy neutrino phenomenology. Despite being Wilsonian irrelevant, the mass-mixing portal can still be efficiently probed at low energies because of its strength *relative* to SM neutrino interactions which proceed through the same dimension-6 contact operators.

There is, however, one unique portal that is dimension-5 and so can come to dominate over SM weak currents at low energies even if it is subdominant at high energies. This is the so-called "dipole portal" which first received substantial attention in the context of the MiniBooNE and LSND anomalies [29–33]. The authors of [34] further pointed out interesting "double-bang" phenomenology that could be probed in experiments such as IceCube. Reference [35] initiated a broad study of the relevant parameter space for a dipole portal, and this was recently complemented by a thorough analysis of low-energy and cosmological phenomena [36]. Since these early studies, the viable parameter space for a neutrino dipole portal has received considerable attention [37–54] and has persisted as a potential explanation of the MiniBooNE excess [40,55].

The interaction Lagrangian for the dipole portal is conventionally taken to be

$$\mathcal{L}_{\rm int} \supset \sum_\alpha d_\alpha F^{\mu\nu} \bar{N} \sigma_{\mu\nu} P_L \nu_\alpha, \tag{2}$$

where d_α is the (flavor-dependent) transition dipole moment between ν_α and the singlet fermion N. In complete generality one could consider a linear combination of magnetic and electric transition dipole portals (see [56] for a recent discussion and [57,58] for related work in the context of angular distributions in HNL decays). It suffices, however, to consider only the magnetic dipole portal as a simplified model in the majority of parameter space, and we restrict our attention to this case here.

Constructing UV completions that yield sizable dipole operators is a nontrivial model building task. One constraint stems from neutrino masses, since loop diagrams involving a photon insertion on the incoming and outgoing neutrino can alter neutrino textures. This can be avoided if N is a Dirac or pseudo-Dirac fermion [35]. Reference [36] discusses possible UV completions connected to leptoquarks and recent B anomalies, and other models have been discussed in [59]. In this paper we work purely at the level of the low-energy Lagrangian Eq. (2)] and remain agnostic to the UV origin of the dipole portal. For the results show below, we consider N to be a Dirac fermion. From a phenomenological standpoint, the primary difference between Dirac and Majorana HNLs is that the Majorana decay length is half of the Dirac decay length [60]. We will show later that the lower bounds we obtain on the model are independent of decay length, so we expect similar bounds for Majorana HNLs.

Finally, we note that HNLs appear generically in dark sector models and that it is natural to consider models in which there are additional light degrees of freedom. While observational evidence demands that low-mass dark sector particles are weakly coupled to the SM, they need not be weakly coupled to one another and it is consistent and arguably generic for there to exist complicated dark sector dynamics (e.g., [2]). A simple example is a model with three HNLs and one massive Z' that interacts with the HNLs via $O(1)$ couplings, but is secluded from the SM except for small kinetic mixing terms with e.g., the SM photon (e.g., [45,61–63]). New dark sector dynamics can modify e.g., decay lengths and couplings to nuclei, however, while details can change, the same basic phenomenology proceeds: neutrinos scatter on nuclei and produce HNLs, and those HNLs decay inside detectors producing a visible decay signature. This is illustrative of the fact that *many* neutrino-portal dark sectors may be efficiently probed via terrestrial upscattering provided the dark sector has a long-lived visibly decaying particle in its spectrum.

In this work we derive new constraints on neutrino portals using existing data by leveraging atmospheric neutrino upscattering (see Fig. 1 for a pictorial description), with our results summarized in Fig. 2. Recent work [60,64] has identified cosmic ray showers as a potentially useful source of HNLs, however, our search strategy differs in that the HNLs are produced via volumetric upscattering within Earth, rather than being produced directly via meson decays in a cosmic rays shower. Because of the large volume of Earth, this search strategy is ideally suited for regions of parameter space in which the HNL decay length is smaller than, or comparable to, the radius of Earth. The signature of interest is the through-going decay of a HNL into some visible SM degrees of freedom and the production mechanism is $\nu A \to N X$ with A some SM particle (typically a nucleus) that is naturally abundant within Earth's mantle and/or core. The treatment of atmospheric neutrino upscattering is considerably more complicated than solar neutrino upscattering which was pursued previously by one of us in [60,64]. The largest technical challenge is that atmospheric neutrinos oscillate over $O(\text{km})$ length scales. This demands a detailed treatment that includes electron number density profiles along arbitrary line segments within Earth. In this paper we develop a Monte Carlo routine that is capable of computing the

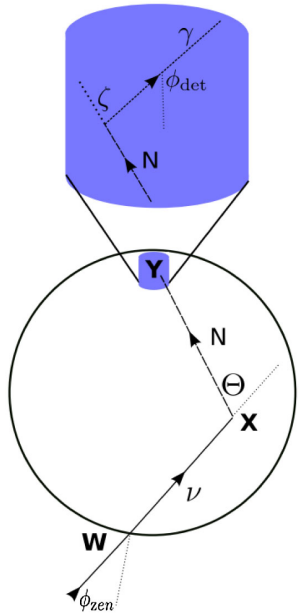

FIG. 1. Schematic of upscattering within Earth and decaying in the detector. A neutrino enters at **W** with angle ϕ_z relative to the vertical. The neutrino scatters into a HNL at **X** with scattering angle Θ. The HNL reaches the detector at **Y**, decays within the detector into a neutrino and a visible photon. The photon is emitted with angle ζ relative to the HNL and detected with angle $\phi_{\rm det}$ relative to the detector.

expected event yield inside a detector, taking into account all relevant physical details.

The rest of this paper is organized as follows. In Sec. II we discuss the upscattering of atmospheric neutrinos. This includes a discussion of neutrino oscillations, atmospheric neutrino intensities, and relevant formulas for upscattering cross sections (both coherent and incoherent). Details of the numerical implementation are deferred to Appendix A. In Sec. II C we discuss the visible signatures of through-going HNLs in large volume detectors. For the dipole portal the signal is always a broad spectrum of photons, whereas for the mass-mixing portal branching ratios vary depending on the HNL mass. Next in Sec. III we derive new constraints on neutrino-portal couplings to HNLs using Super-Kamiokande (SK or Super-K) data and discuss potential improvements with both Hyper-Kamiokande and DUNE in Sec. IV. Finally, in Sec. V we summarize our findings and discuss potential future directions.

II. UPSCATTERING IN EARTH

Atmospheric neutrinos supply a broadband spectrum of electron and muon flavor neutrinos ranging from ∼100 MeV up to ∼100's of GeV. At these energies the neutrinos pass through Earth without scattering, but do undergo substantial flavor oscillations that depend non-trivially on the matter profile encountered by the neutrinos in transit. At a typical point inside Earth, this results in a quasi-isotropic intensity of neutrinos with a $O(1)$ contributions from ν_e, ν_μ, and ν_τ with a broad range of energies as described above. In what follows we outline how to formalize the problem of atmospheric neutrino upscattering $\nu A \to NX$, with A a SM nucleus and X some SM final state particles.

For our upscattering formalism, we begin with the incoming flux of atmospheric neutrinos. The flux of these neutrinos is sensitive to the neutrino energy and the zenith angle relative to the neutrino entry point.[2] For flavor-dependent couplings we include neutrino oscillations, which are affected by the matter profile between the entry position **W** and the interaction point **X**. The result is an angle- and energy-dependent neutrino intensity $\mathcal{I}_{\nu_\alpha}(E_\nu, \Omega_\nu, \mathbf{X})$ that depends on the neutrino flavor α and the position inside Earth, **X**. This intensity can be related to the standard atmospheric neutrino intensity of flavor β, I_{ν_β}, (at the surface) via

$$\mathcal{I}_{\nu_\alpha}(E_\nu, \Omega_\nu, \mathbf{X}) = P_{\alpha\beta}(\mathbf{X}, E_\nu, \Omega_\nu) I_{\nu_\beta}(E_\nu, \cos\phi_{\rm zen}), \quad (3)$$

where a sum over β is implied, and $\cos\phi_{\rm zen}$ is chosen so that the neutrino points from **W** to **X** (see Fig. 1). Neutrino oscillation probabilities, denoted by $P_{\alpha\beta}$ for $\nu_\beta \to \nu_\alpha$, depend on the position inside Earth and the angle of incidence since these two parameters determine the neutrino's path through Earth. The zenith angle at which the neutrino is produced also depends on both **X** and Ω_ν. The neutrino oscillations must be computed separately for each angle, energy, and point inside Earth. In what follows we take recent best fit values from the NuFit Collaboration [71]: $\Delta m^2_{21} = 7.42 \times 10^{-5}$ eV^2, $\Delta m^2_{31} = 2.52 \times 10^{-3}$ eV^2, $\theta_{12} = 33.44°$, $\theta_{13} = 8.57°$, $\theta_{23} = 49.2°$, and $\delta_{CP} = 197°$. The effect of varying neutrino oscillation parameters within their allowed range of values produces only a small effect. This is because the flux of HNLs arriving at the detector depends on the volume-averaged oscillation probabilities weighted by the broadband atmospheric flux. The result therefore samples a wide range of L/E_ν and is relatively insensitive to e.g., δ_{CP} and the mass-mixing hierarchy.

While most of the atmospheric neutrino flux has energies of 100's of MeV, the flux extends to 10's of TeV. Momentum transfers can then be much larger than the scale of nuclear coherence $Q_{\rm coh} \sim 100$ MeV such that scattering will not be entirely coherent. Instead, the cross section can be composed of a coherent and incoherent piece $d\sigma = d\sigma_{\rm coh} + d\sigma_{\rm in.}$ where $d\sigma_{\rm coh} \sim O(Z^2, Q_w^2)$ and $d\sigma_{\rm in.} \sim O(Z, Q_w)$ with Z an Q_w the electric and weak charge of the nucleus. The former is relevant for the dipole portal and the latter is relevant for the mass-mixing portal. The

[2]In general one could also consider neutrino fluxes that depend on latitude and longitude, however, the Honda fluxes [70] are computed only at a few select locations and so we treat cosmic ray production identically at all locations on Earth's surface.

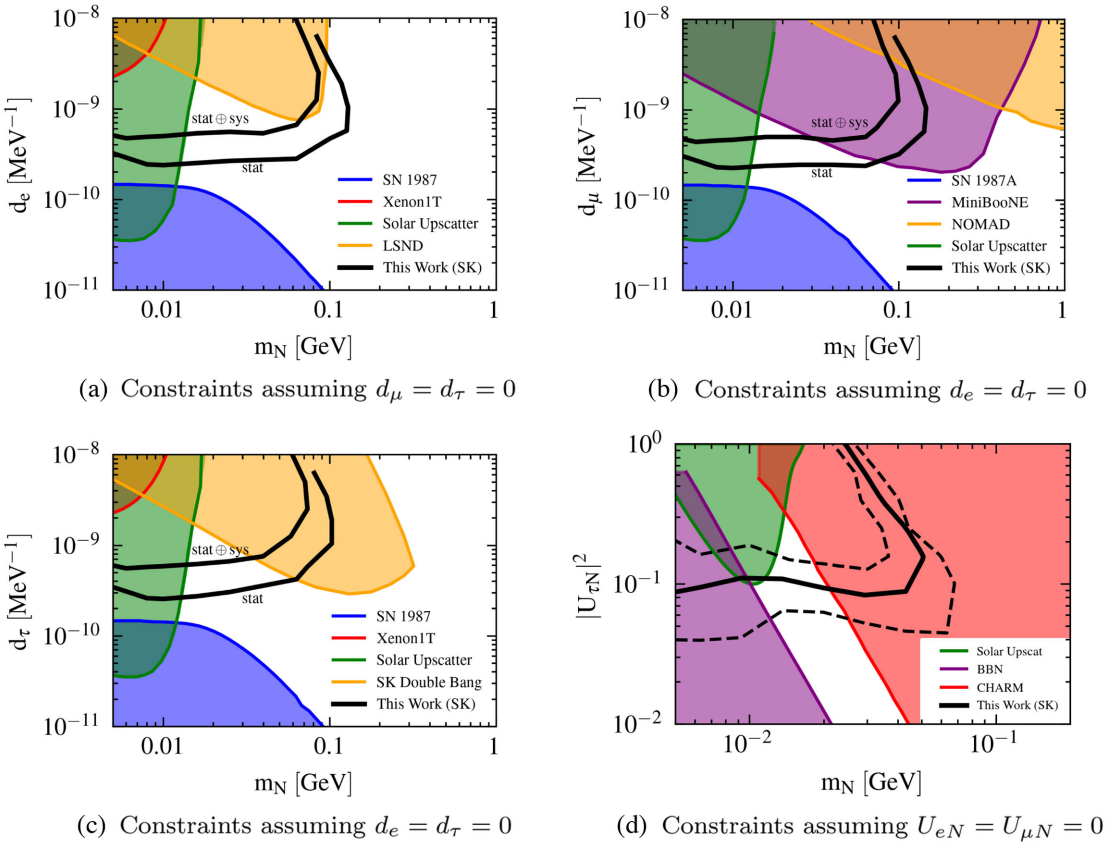

(a) Constraints assuming $d_\mu = d_\tau = 0$

(b) Constraints assuming $d_e = d_\tau = 0$

(c) Constraints assuming $d_e = d_\tau = 0$

(d) Constraints assuming $U_{eN} = U_{\mu N} = 0$

FIG. 2. Comparison of our dipole-portal limits (a)–(c) and mass-mixing limit for $|U_{\tau N}|^2$ (d) vs existing limits derived in the literature (for a helpful compilation of *projected* sensitivities see [42]). We have included two bounds from Super-Kamiokande for the dipole portal: one where $\sigma_{\rm sys} = 0$ and another where $\sigma_{\rm sys}$ is 5% of the background events. Notice that due to atmospheric neutrino oscillations averaged over the interior of Earth our constraints are flavor independent up to an $O(1)$ factor. Constraints from NOMAD (μ-only) are taken from [34,65], MiniBooNE (μ-only), supernova bounds (assumed flavor democratic), and LSND constraints are taken from [35], and solar constraints are taken from [60]. The τ-only mass-mixing constraints are taken from [47,64,66–69]. The dashed lines in (d) are meant to illustrate the theoretical uncertainty in the production rate due to incoherent scattering on nuclei. The lower (upper) dashed line is where we double (halve) the contribution due to incoherent scattering. The coherent contribution (which is nearly free of nuclear uncertainties) guarantees irreducible flux atmospheric upscattered HNLs.

coherent contribution can be reliably treated working in the infinite mass limit because nuclear form factors ensure that $|Q| \sim 0.3$ GeV, whereas nuclei are generically heavy $M_A \sim 30$ GeV such that nuclear recoil energies are small $T_R \sim Q^2/2M_A \ll E_\nu$.

In general the upscattering cross section will depend on both the scattering angle and HNL energy $\mathrm{d}^2\sigma/\mathrm{d}\cos\Theta \mathrm{d}E_N$. We are interested in angles Θ, such that the resulting HNL is directed toward the detector. When considering coherent scattering, the nuclear recoil can be neglected such that

$$\left[\frac{\mathrm{d}^2\sigma}{\mathrm{d}\cos\Theta \mathrm{d}E_N}\right]_{\rm coh} = \frac{\mathrm{d}\sigma}{\mathrm{d}\cos\Theta}\delta(E_N - E_\nu). \tag{4}$$

For elastic scattering on *free* nucleons, recoil effects must be included and the delta function instead relates E_N as a function of both E_ν and $\cos\Theta$. In this work we include the contribution from coherent scattering and incoherent scattering on the constituent nucleons. We model the incoherent contribution as if the scattering took place on free nucleons and neglect detailed nuclear effects. In models where the upscattering is dominated by coherent scattering (e.g., the dipole portal) the nuclear uncertainties are drastically reduced. For the mass-mixing portal we find that incoherent scattering provides an $O(1)$ contribution to the total rate and treat the theory uncertainty from nuclear effects conservatively [see Fig. 2(d)].

The HNL created in this interaction is unstable, with a decay length of

$$\lambda = \gamma\beta\tau, \tag{5}$$

where τ is the characteristic decay time in the rest frame of the HNL. Given the decay length λ, the probability for a HNL produced at a location $\mathbf{X}$ directed toward our detector located at $\mathbf{Y}$ to decay visibly within the fiducial volume, of length ℓ and area $A_\perp$ is

$$P_{\rm vis} = B_{\rm vis} \times \exp\left(-\frac{|\mathbf{X}-\mathbf{Y}|}{\lambda}\right)(1-e^{-\ell/\lambda}), \quad (6)$$

where $B_{\rm vis} = \Gamma_{N\to\rm vis}/\Gamma_N$ is the branching ratio to visible SM decay products (an experiment and search strategy-dependent quantity). The probability of a HNL being directed toward the detector is proportional to the solid angle of the detector as seen from the point of emission, $\Omega_{\rm det} \sim A_\perp/|\mathbf{X}-\mathbf{Y}|^2$. We note that in the limit $\lambda \gg \ell$ we may approximate $1-e^{-\ell/\lambda} \approx \ell/\lambda$ such that the overall rate scales as the volume of the detector $V = A_\perp \ell$. For $\lambda \sim \ell$ the rate will depend somewhat on the geometry of the detector and so the ceiling of our constraints will be modified by an $O(1)$ number; because this region is already ruled out by complementary search strategies this is not important, except perhaps for electron-only coupled dipole portals [see Fig. 2(a)]. Putting everything together, the event rate for HNLs produced by a ν_α neutrino portal (with $\alpha \in \{e,\mu,\tau\}$) to decay visibly inside the fiducial volume of a detector is given by

$$\frac{dR_{N\to\rm vis}}{dE_N} = \int_\oplus d^3X \left[\int dE_\nu \int d\Omega_\nu \sum_i n_i(\mathbf{X}) \frac{1}{4\pi|\mathbf{X}-\mathbf{Y}|^2} \mathcal{I}_{\nu_\alpha}(E_\nu,\Omega_\nu,\mathbf{X}) \frac{d^2\sigma_i}{d\cos\Theta dE_N}\right] A_\perp P_{\rm vis}(E_N,|\mathbf{X}-\mathbf{Y}|). \quad (7)$$

The term in square brackets is the differential flux of HNLs per unit volume produced at location $\mathbf{X}$ and the factor $P_{\rm vis}$ weights the spectrum by the probability of decay within the detector. The event spectrum for a given visible decay product can be found by folding the differential rate dR/dE_N computed using Eq. (7) with the spectrum of daughter particles produced in the lab frame by a HNL with energy E_N.

Equation (7) cannot be calculated analytically for simple matter profiles due to the complex dependence of the oscillated neutrino intensity as a function of $\mathbf{X}$. Even without oscillations, a realistic density and composition profile of Earth demands a numerical treatment. We have developed a purpose built Monte Carlo program capable of solving Eq. (7) efficiently using conditional importance sampling. The details of our implementation are discussed in Appendix A, however, we briefly sketch the procedure here. First, we generate an ensemble of neutrino energies by importance sampling an approximate atmospheric neutrino flux curve. For each neutrino energy we calculate the maximum HNL decay length, which corresponds to the case when $E_N = E_\nu$ such that $\lambda_{\rm max} = \lambda(E_N = E_\nu)$. We then sample a position inside Earth $\mathbf{X}$ from an exponential distribution defined relative to the detector. At each point $\mathbf{X}$ the density and composition of Earth is computed. For each production mechanism (e.g., coherent vs incoherent scattering off ^{56}Fe and ^{16}O), we generate a random initial neutrino angle (defined relative to $\mathbf{Y}-\mathbf{X}$) using a non-uniform sampling that accounts for correlations induced by the differential cross section[3] $d\sigma_i/d\cos\Theta$. Given the incident neutrino angle, we then propagate backward to the point on Earth's surface where the neutrino would have originated $\mathbf{W}$, and we calculate the zenith angle relative to Earth's tangent at that point. The neutrino intensity is then calculated using NuFlux [74] with E_ν taken from the first step and at the required zenith angle to propagate from $\mathbf{W}$ to $\mathbf{X}$. All events are saved in an event record, with appropriate weights accounting for the various terms in Eq. (7). Finally, in a postprocessing stage we calculate the relative weights for the various neutrino flavors at the location $\mathbf{X}$ by numerically solving the Schrödinger equation along the line segment connecting the upscattering location $\mathbf{X}$ to the neutrino point of origin at Earth's surface. This is done self-consistently using the same density and composition profile as was used to generate the upscattering events.

We now specialize our discussion to the relevant neutrino portals discussed herein.

A. Dipole portal

For the dipole portal, the visible decay signal is $N \to \gamma\nu$ with a branching ratio of BR = 1. The analysis is consequently straightforward. The decay length of the HNL is given by

$$\lambda = \frac{4\pi}{d^2 m_N^3}\gamma\beta, \quad (8)$$

which is comparable to the size of Earth for much of the parameter space of interest.

For a neutrino dipole portal, coherent scattering on nuclei is the dominant upscattering process for all energies. The upscattering cross section assumes a simple form when one works in the large mass limit and drops all mass-suppressed effects including nuclear recoil corrections and contributions from a nuclear magnetic dipole moment. This is a valid approximation because the nucleus' charge form factor ensures that $\mathbf{Q} \ll 300$ MeV, such that recoil corrections are always small. The resulting differential cross section is of the form

$$\frac{d\sigma_{\rm coh}}{d\mathbf{Q}^2} \sim \frac{4Z^2\alpha d^2}{\mathbf{Q}^2}|F(\mathbf{Q}^2)|^2 \times \left(1-\frac{m_N^2}{4E_\nu^2}-\frac{m_N^4}{E_\nu^2\mathbf{Q}^2}\right). \quad (9)$$

[3]For highly forward scattering these correlations can make certain numerical methods (e.g., VEGAS) highly inefficient [72,73]. By "working backward" from the detector to the source of neutrinos we efficiently account for these correlations.

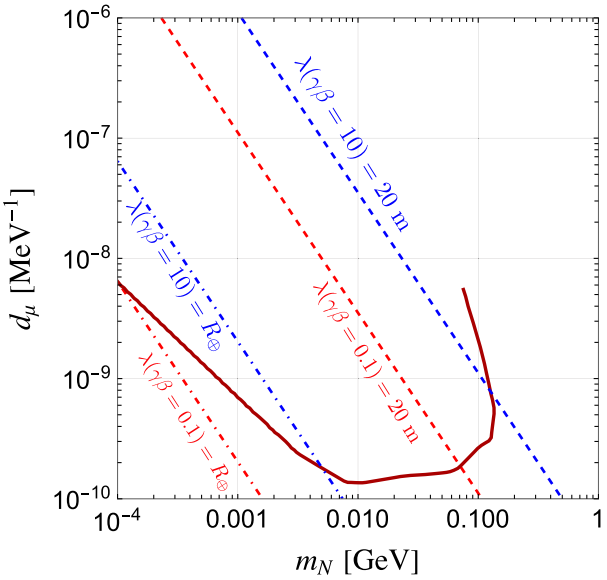

FIG. 3. Combined exclusion contours ignoring oscillations, along with relevant decay lengths. This plot is for the flavor-independent dipole coupling ($d_e = d_\mu = d_\tau$).

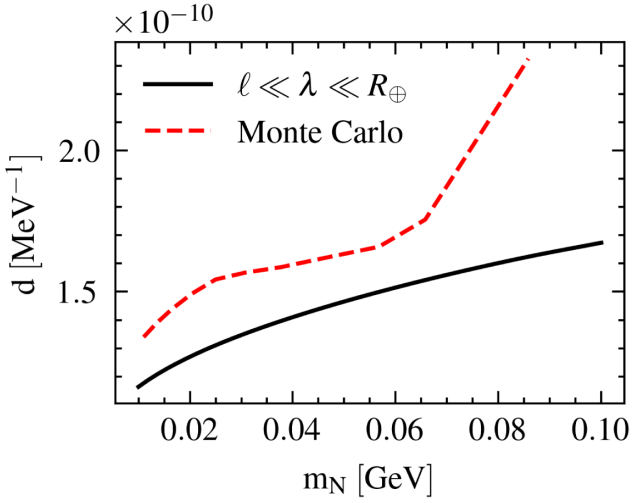

FIG. 4. Flavor-independent curves corresponding to 197 HNL events at Super-Kamiokande with 5326 days of data using the approximation from Eq. (11) and the Monte Carlo simulation. In the approximation, we consider Earth as composed entirely of silicon with a density of 5 g/cm^3.

The angular dependence $\mathrm{d}\sigma/\mathrm{d}\cos\Theta$ can be obtained by a simple change of variables. The charge form factor of each nucleus is modeled as a Helm form factor with parameters fitted to the tabulated two-parameter Fermi distributions from [75] (see Appendix B 3 for more discussion).

Although it is subdominant to the coherent contribution, we also include an incoherent sum over nucleons in our model of upscattering. This cross section is given by $\mathrm{d}\sigma_A = Z\mathrm{d}\sigma_p + (A-Z)\mathrm{d}\sigma_n$ with the proton and neutron cross sections parametrized in terms of standard Dirac and Pauli form factors.

We can see in Fig. 2 that our dipole coupling bounds have a relatively flat region in d when m_N is between 0.01 and 0.08 GeV. In Fig. 3, we see that this flat region corresponds to decay lengths satisfying the hierarchy $\ell \ll \lambda \ll R_\oplus$. This bound can be estimated through a relatively simple approximation: treat Earth as being of a constant density composed of a single element, consider the neutrino flux as isotropic, ignore angular dependence on the cross section, consider elastic scattering such that $E_\nu = E_N$, and set all terms of $O(\ell/\lambda)$ and $O(\lambda/R_\oplus)$ to zero. Within this approximation, we find

$$\frac{\mathrm{d}R_{N\to\mathrm{vis}}}{\mathrm{d}E_N} = \frac{nV_{\mathrm{det}}}{2} I_\nu(E_N)\sigma(E_N)f_{\mathrm{vis}}(E_N), \tag{10}$$

where f_{vis} is the fraction of HNL decays in our detector that are in the visible energy range. Here, the only dependence on the transition dipole moment appears in the cross section as a d^2 (the rate is independent of the decay length for $\ell \ll \lambda \ll R_\oplus$). We can define $\tilde{\sigma} = \sigma/d^2$, and then our estimate for the floor of our constraint is

$$d(m_N) = \sqrt{\frac{2R^{\mathrm{exp}}_{N\to\mathrm{vis}}}{nV_{\mathrm{det}}\int \mathrm{d}E_N I_\nu(E_N)\tilde{\sigma}(E_N)f_{\mathrm{vis}}(E_N)}}, \tag{11}$$

where $d(m_N)$ is an estimate for the floor of our constraint as a function of m_N and $R^{\mathrm{exp}}_{N\to\mathrm{vis}}$ is the rate of visible energy deposition that can be excluded by the experiment under consideration. In Fig. 4, we see that this approximation closely matches the true bounds that we get for the full Monte Carlo, meaning that this approximation can be used to see how the lower bound will scale with exposure time, volume, decreased background, etc. Since this approximation ignores decay length, it should also be valid for setting approximate bounds on Majorana HNLs, which have half the decay length of Dirac HNLs.

B. Mass-mixing portal

The mass-mixing portal is more complicated phenomenologically because production cross sections rise with energy, and for $m_N \gtrsim m_\pi$ many new hadronic decay channels open. We have included many of these details in our simulation, however, *a posteriori* it is clear that searches relying on terrestrial upscattering are only competitive with existing constraints for masses below the pion threshold. We therefore focus our discussion on the case of the decay channel $N \to e^+e^-\nu$ which is the only visible decay mode for $m_N \leq 135$ MeV.

The decay of a HNL to an e^+e^- pair depends on the flavor structure of the mass-mixing portal and the flavor of the invisible SM neutrino. These effects introduce an $O(1)$ prefactor that depends on the final state which can be found in [22,24,76], however, the dominant effect is the muon decaylike formula for the partial width

$$\Gamma_{e^+e^-\nu} = \frac{G_F^2 m_N^5 |U|^2}{192\pi^3} \times O(1). \tag{12}$$

The result is that HNL decay lengths are extremely long for low masses and can easily exceed the radius of Earth by orders of magnitude. In this regime terrestrial upscattering offers substantial benefits over traditionally laboratory-based searches and can offer leading sensitivity on $|U_{\tau N}|^2$.

HNLs can always decay to three neutrinos, $N \to \nu\nu\nu$ for any nonzero mixing angle. The result is a branching ratio that is $O(10\%)$ for $N \to \nu e^+ e^-$ for all HNL masses below the pion threshold. We include this effect in our simulations computing the full decay length and taking $B_{\rm vis} = \Gamma_{e^+e^-\nu}/\Gamma$.

HNL upscattering proceeds via the weak neutral current and for the relatively low HNL masses that we focus on here all of the coherent (i.e., CEvNS), quasielastic, and deep inelastic scattering contribute to the upscattering yield. We find that for regions of parameter space where atmospheric upscattering is competitive that the scattering mechanisms are dominantly coherent and incoherent scattering on nucleons, with deep inelastic events contributing only a few percent to the total flux.

The coherent contribution is relatively insensitive to the nuclear species and can be calculated from first principles. We model the weak nuclear form factor by setting it equal to the charge nuclear form factor. Incoherent scattering on nuclei is modeled as described above for the dipole portal. This neglects all effects of nuclear structure and we therefore expect a sizable theoretical error from our modeling. Unlike the dipole-portal case, we find that incoherent scattering makes up roughly two-thirds the total upscattered flux. Owing to its relative importance, we have included "error bands" in Fig. 2 in which the incoherent scattering cross section has been doubled and halved, respectively; we believe this to be a conservative overestimate of the theoretical uncertainty.

C. Decays inside the detector

In the presentation above we have outlined how to calculate the flux of unstable particles arriving at a given large volume detector. This flux is not directly visible, and the bona fide observable is the energy and angular distribution of a HNL's visible daughter particles. For illustration, we discuss the case of a dipole-portal decay $N \to \nu\gamma$ in detail below. The case of a three-body decay, as in $N \to \nu e^+ e^-$ is qualitatively similar, but slightly more involved due to the three-body final state. The details of the decay distribution do not substantially impact our rate-only estimate, although their details may be relevant for future searches that we outline in Sec. IV.

In the case of the dipole portal, when the HNL decays, it decays into a photon and neutrino. The angular distribution of a dipole-mediated decay in the HNL rest frame depends on the level of CP violation [56,57,77–79], with $d\Gamma/d\cos\zeta' \sim 1 + \alpha\cos\zeta'$ and $\alpha \in [-1, 1]$ and ζ' the angle between the photon and the HNL polarization. For simplicity, we take $\alpha = 0$ such that the decays are isotropic. Our sensitivity is only mildly sensitive to this choice; $\alpha > 0$ leads to a somewhat harder photon spectrum in the lab frame, while $\alpha < 0$ leads to a somewhat softer spectrum (see e.g., related discussion in [60]). In the rest frame, $E_{\nu,\rm rest} = E_{\gamma,\rm rest} = E_N/2$, and this leads to the following lab frame kinematic variables:

$$\tan(\zeta_{\rm lab}) = \frac{m_N}{E_N} \frac{\sin(\zeta')}{\cos(\zeta') + \sqrt{1 - m_N^2/E_N^2}}, \tag{13}$$

$$E_{\gamma,\rm lab} = \frac{E_N}{2}\left(1 + \cos(\zeta')\sqrt{1 - \frac{m_N^2}{E_N^2}}\right). \tag{14}$$

A flat (i.e., isotropic) distribution in $\cos\zeta'$ results in a "box distribution" for $E_{\gamma,\rm lab}$ ranging between $[E^{(-)}_{\gamma,\rm lab}, E^{(+)}_{\gamma,\rm lab}]$ where $E^{(\pm)}_{\gamma,\rm lab} = \frac{1}{2}E_N(1 \pm \sqrt{1 - m_N^2/E_N^2})$. Knowing the initial momentum of the HNL, we can sample $\cos\zeta'$ uniformly between $[-1, 1]$ and generate a random sample of angles of the detected photon relative to the horizon at the detector $\phi_{\rm det}$.

III. SUPER-KAMIOKANDE CONSTRAINTS

We now turn to our analysis of public data from Super-Kamiokande, which when coupled with our Monte Carlo simulation allows us to set new limits on neutrino-portal couplings. SK is a large volume (22.5×10^3 m^3 fiducial volume) Cherenkov detector whose primary background is the scattering of atmospheric neutrinos passing through the detector. It is well suited to search for through-going HNL decays and has a large statistical sample of atmospheric neutrino events which can be used to set limits on the rate of visible HNL decay [80,81].

The SK Collaboration classifies events as sub-GeV (30 MeV $< E_{\rm vis} <$ 1.33 GeV) and multi-GeV ($E_{\rm vis} >$ 1.33 GeV) with subclassifications for each event type. In the sub-GeV sample, events are classified as e-like, μ-like, or π^0-like, single ring or two ring, and 0-decay-e, 1-decay-e, or 2-decay-e. The decay-e classification is meant to capture Michel electrons from muon decay, while the particle identification is based on characteristic Cherenkov ring patterns of each particle. The multi-GeV sample is split into partially contained and fully contained, the former applying exclusively to muon events. In the fully contained sample, events are classified as single ring or multiring and are then further subdivided as ν_e-like, $\bar{\nu}_e$-like, or μ-like. The ν_e- vs $\bar{\nu}_e$-like samples are defined by a cut on the number of decay-e events which ultimately stem from a $\nu_e n \to e^-\pi^+ n$ interaction with subsequent pion decay at rest, followed by muon decay [82]. Not all ν_e interactions produce a π^+ and so there is substantial cross-contamination

between the two samples; by way of contrast the μ-like sample is relatively pure.

In what follows we describe a simple rate-only analysis based on the published results in [82]. For each model we focus on the relevant experimental signature and use the experimental collaboration's Monte Carlo prediction as the expected Poisson mean of the event sample. Given their observed data, we then set limits at the 95% confidence level on the number of allowed events in the energy range as defined by the experiment. We consider both systematics and statistically limited searches with a conservative estimate of a 5% systematic uncertainty on the collaboration's Monte Carlo prediction for their sub-GeV sample of 0-decay-e events.

A. Dipole portal

The dipole portal's only signature is a single photon which will be classified as an e-like 0-decay-e signature in the sub-GeV analysis and as a fully contained $\bar{\nu}_e$-like event in the multi-GeV sample. The energy distribution of photons is broad for all HNL masses but its precise shape depends on both m_N and d. The multi-GeV and sub-GeV samples therefore provide complementary tools with which to probe the HNL parameter space.

We set limits by taking the union of the excluded regions from the multi-GeV and sub-GeV analyses separately and these are shown in Fig. 5. We note that the constraints cross around $d \simeq 5 \times 10^{-9}$ MeV^{-1}, with the multi-GeV search dominating for larger d and the sub-GeV dominating below. We consider $d_e = d_\mu = d_\tau = d$ (flavor-independent) and

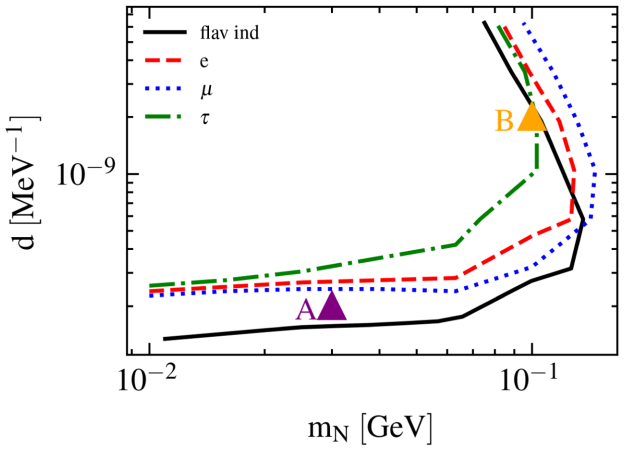

FIG. 5. Exclusion contours assuming a statistically limited search (i.e., $\sigma_{\rm sys} = 0$) from Figs. 2(a)–2(c) and the equivalent constraint for a flavor-independent (flav ind) dipole portal. Our constraints are only moderately sensitive to neutrino flavor due to substantial oscillations within the interior of Earth. Point A is representative of parameter space that is dominated by the sub-GeV sample at Super-K. Point B is representative of a point in parameter space that is dominated by the multi-GeV sample. We discuss this further in Sec. IV and show distributions for point A in Figs. 6 and 8 and point B in Figs. 7 and 9.

flavor-dependent couplings accounting for neutrino oscillations in each case. Based on Table II of [82], we assume a Poisson mean from the collaboration's Monte Carlo simulation of $\mu_{\rm MC} = 10266$ sub-GeV 0-decay-e events while the observed count is $N_{\rm obs} = 10294$.

It is tempting, given the close agreement between Monte Carlo and observation, to infer that systematic uncertainties on the Monte Carlo prediction are fully under control, however, the Super-Kamiokande Monte Carlo is tuned to their data to self-consistently determine, e.g., the atmospheric flux normalization. In the presence of new physics this tuning could be compromised and so it is important to estimate a systematic uncertainty on an experiment such as Super-Kamiokande. First, note that while the overall normalization of the atmospheric flux is poorly constrained, the ν_e: ν_μ ratio is known to within a few percent [70,82]. Therefore the flux normalization at Super-Kamiokande can be fixed using muon-exclusive subsamples, and the electron flux can be subsequently inferred. Second, it is worth noting that the sub-GeV 0-decay-e bin of the Super-Kamiokande dataset is relatively insensitive to neutrino oscillations, and its background modeling is therefore reasonably robust. Quantitatively, one can compare the predicted flux with and without oscillations from Fig. 14.4 of [83]; the flux changes by only 2.7%. We therefore conclude that a 5% systematic uncertainty can be conservatively applied to the Super-Kamiokande (Super-K) Monte Carlo prediction of the 0-decay-e sub-GeV background from atmospheric ν_e scattering.

For finding constraints, we take the statistical uncertainty as $\sigma_{\rm stat} = \sqrt{\mu_{\rm MC} + \mu_{\rm HNL}}$. We take a conservative upper bound on the systematic uncertainty at $\sigma_{\rm sys} = 0.05\mu_{\rm MC}$. We then solve $P(x \leq N_{\rm obs}|\mu, \sigma) = 0.05$ where our probability distribution function is $(2\pi\sigma)^{-1/2} \exp\left(\frac{(x-\mu)^2}{2\sigma}\right)$ and $\mu = \mu_{\rm MC} + \mu_{\rm HNL}$ and $\sigma = \sqrt{\sigma_{\rm stat}^2 + \sigma_{\rm sys}^2}$. For $\sigma_{\rm sys} = 0$, we find that $\mu_{\rm HNL} = 197$ is excluded at 95% C.L.; this corresponds to the number of events per 328 kt-yr (corresponding to 5326 live days at Super-K). For $\sigma_{\rm sys} = 0.05\mu_{\rm MC}$, we find that our 95%-C.L. bound now corresponds to $\mu_{\rm HNL} = 893$. For the multi-GeV analysis we take the $\bar{\nu}_e$-like sample which has $\mu_{\rm MC} = 2194$ and $N_{\rm obs} = 2142$ for a 328 kt-yr exposure. Following the same procedure as above, the $\sigma_{\rm sys} = 0$ 95%-C.L. bound is $\mu_{\rm HNL} = 26$ and the $\sigma_{\rm sys} = 0.05\mu_{\rm MC}$ 95%-C.L. bound is $\mu_{\rm HNL} = 145$. It is worth noting that the excluded number of excess events is determined solely by uncertainties in the rate of Standard Model events at Super-K. Uncertainties in our beyond the standard model (BSM) theory only affect how we translate these exclusion bounds into parameter space. We also expect that any uncertainties in our theory are accounted for by our conservative estimate on the Super-K uncertainty.

Using our Monte Carlo integrator, we compute the rate of HNLs passing through and decaying within the detector.

The photon spectrum is generated using the lab frame decay distribution of the HNL. For flavor-dependent dipole couplings we reweight the ensemble of Monte Carlo events by adjusting the intensity of neutrinos at the upscattering location according to the oscillation probabilities computed along the line segment connecting the upscatter location to the position on Earth's surface above which the atmospheric neutrino is produced. Photon detection efficiencies are taken to be unity, $\epsilon_\gamma = 1$, which we believe to be reasonable as Super-K can reach 100% trigger efficiency on events with 4.49 MeV of energy [84], and our photon energies are well above this. The photon spectrum is integrated from $E_\gamma = 30$ MeV to $E_\gamma = 1.33$ GeV for the sub-GeV sample and from $E_\gamma = 1.33$ GeV to the highest energy in the Monte Carlo sample for the multi-GeV sample.

B. Mass-mixing portal

For the mass-mixing portal we focus our analysis on $N \to e^+e^-\nu$ which is the only visible decay mode for $m_N \lesssim 130$ MeV and contributes for all HNL masses. As we will show the only region in which terrestrial upscattering can compete with fixed target experiments is in the low-mass regime and so this suffices for our purposes.

An e^+e^- pair will appear as highly collimated and result in an electromagnetic shower that is difficult (or impossible) to distinguish from a single electron or single photon. The HNLs are sufficiently boosted such that wide-angle e^+e^- pairs are a nonissue and the decay signature maps onto the same search channels as the single photon analysis. We can therefore take the rate-only exclusions from above an apply them directly to the mass-mixing portal. The sub-GeV sample provides the best sensitivity to HNL mass mixing over the full range of parameter space and we find that new regions of parameter space for τ-coupled HNLs can be probed with existing Super-Kamiokande data.

For our upscattering simulation we include coherent, quasielastic, and deep inelastic scattering channels. We do not include resonance production, nor do we account for nuclear structure (e.g., Pauli blocking, giant dipole resonances, etc.). We note that in our region of sensitivity, incoherent scattering off of nucleons is the dominant contribution (contributing to around 2/3 of the rate). Coherent scattering contributes to around 25% of the total rate, and deep inelastic scattering contributes to less than 10% of the rate.

C. Scaling with increased sensitivity

Before moving on to considering future experiments, let us discuss how the constraints described above scale with increased sensitivity. Importantly, the rightmost boundary of our exclusions corresponding to an upper bound on m_N is set by our *sensitivity* rather than by any kinematic thresholds. This is because the flux of atmospheric neutrinos is broad and there is no fundamental limitation on the mass of HNLs which can be produced. As sensitivity improves, either by collecting more data, improving background discrimination, or by leveraging new detector technologies, heavier HNLs can be probed. Furthermore, in the regions of parameter space highlighted in Fig. 3, limits on the dipole coupling scale as $d \sim (\text{sensitivity})^{1/2}$ which is extremely advantageous relative to the naive scaling of $d \sim (\text{sensitivity})^{1/4}$ that one would expect in the long-lifetime limit. Taken together, this suggests that improved sensitivity using atmospheric upscattering as a source of HNLs has a high return on investment.

IV. SEARCH STRATEGIES AT FUTURE EXPERIMENTS

In this section we discuss how to improve future searches for HNLs. All of the exclusion contours in this work are based exclusively on the simple rate-only estimates of the previous section and the reader may view the following discussion as an outlook toward future improvements. Our Monte Carlo routine can generate kinematic distributions such as the energy and zenith angle of the HNL's decay products, and these can be leveraged to improve signal to background ratios. We also discuss potential improvements in background rejection using different detector technology (e.g., liquid scintillator and/or liquid argon time projection chambers instead of a Cherenkov detector) and the impact of a larger fiducial volume in a detector such as Hyper-Kamiokande (HK or Hyper-K).

Let us begin by discussing improvements that can be had by taking into account the energy and angular distributions of the observed photons. For illustration, let us examine two dipole model parameter points which are at the Super-Kamiokande exclusion boundary: the two points marked by triangles in Fig. 5. Recall that these searches exclude a window of couplings, originating from the requirement that decay lengths satisfy $10\ \text{m} \lesssim \lambda \lesssim R_\oplus$. Consequently we will refer to the "floor" and "ceiling" of the coupling exclusion region.

Let us first examine the angular and energy distributions of the detected photons from a parameter point on the floor of the exclusion region, $m_N = 0.03$ GeV and $d_e = 2 \times 10^{-10}\ \text{MeV}^{-1}$. We include an example of these distributions on our lower bound for electron-flavor coupling in Fig. 8. We see the angular distribution highly favors angles less than $\pi/2$, corresponding to upward-going photons in our case. Since the photon direction is highly correlated with the HNL direction, this means most of our signal comes from HNLs produced below the detector. Our decay length is large for these parameters, so there is far more volume available for scattering below the detector than above it. The energy distribution is peaked at lower energies both as a consequence of the atmospheric neutrino flux, which falls off quickly with energy, and because of the

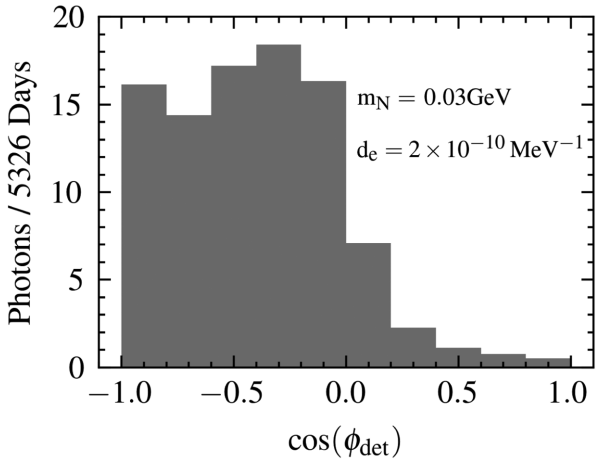

FIG. 6. Angular distribution of the detected photons for point A in Fig. 5 ($m_N = 0.03$ GeV and $d = 2 \times 10^{-10}$ MeV^{-1}). At low HNL masses and small dipole couplings, the angular distribution of photons is primarily up-going ($\cos\phi_{\mathrm{det}} < 0$). This can be used in future searches to cut backgrounds.

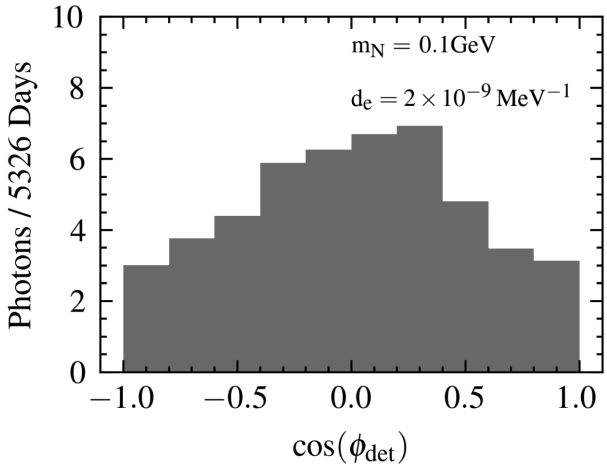

FIG. 7. Angular distribution of the detected photons for point B in Fig. 5 ($m_N = 0.1$ GeV and $d = 2 \times 10^{-9}$ MeV^{-1}). The angular spectrum is relatively flat, because at shorter decay lengths, the mountain above Super-Kamiokande contributes an $O(1)$ fraction of the upscattering events.

skewed distribution of photons from the decay of relativistic HNLs [see discussion near Eq. (15)]. The most probable photon energy in the lab frame is given by one-half the HNL's energy. At low HNL masses, almost all of the atmospheric neutrino flux is capable of producing HNLs. For coherent scattering $E_N = E_\nu$, and since the atmospheric neutrino flux falls like a power law the HNL inherits this feature resulting in lower energy photons.

The angular distribution of observed events at Super-Kamiokande is nearly uniform [80]. Therefore, we can choose to only look at upward-going events and cut our background in half while keeping our signal virtually unchanged. We expect that this will extend our lower bound of d by a factor of $2^{1/4}$, as we will need $\sqrt{1/2}$ as many events to reach the same level of uncertainty, and the number of upscattering events goes as d^2.

Now let us turn our attention to a parameter point on the ceiling of the excluded region. In this case, the energy and angular distributions are qualitatively different. We show examples of the electron-flavor case for $m_N = 0.1$ GeV and $d_e = 2 \times 10^{-9}$ MeV^{-1} (Figs. 7 and 9). We see that the photons are now more uniformly distributed in angle. This is because the decay length is now much shorter than the depth of the detector, so the volume available for upscattering is approximately spherical, and we expect our flux of HNLs at the detector to be roughly uniform in angle. We see that there is a slight peak near $\cos\phi_{\mathrm{det}} = 0$, since more neutrinos come from the horizontal direction than from the vertical.

The energy distribution for HNLs with shorter decay lengths (corresponding to large masses and strong couplings) is nearly uniform in the sub-GeV sample at Super-Kamiokande. This can be understood as follows: the flux of HNLs roughly mimics the flux of atmospheric neutrinos and so in the sub-GeV regime is relatively flat. The flux of photons is given roughly by $\mathrm{d}N/\mathrm{d}E_\gamma \sim A_\perp \lambda P_{\mathrm{vis}}(\lambda,\ell) \int \mathrm{d}E_N \Phi(E_N)\mathrm{Box}(E_\gamma|E_N)$ with $P_{\mathrm{vis}}(\lambda,\ell) = 1 - \exp(-\ell/\lambda)$. For long decay lengths, we find $\lambda P_{\mathrm{vis}} \approx \ell$ and the energy distribution is given by $\mathrm{d}N/\mathrm{d}E_\gamma \sim V_{\mathrm{det}} \times \int \mathrm{d}E_N \Phi(E_N)\mathrm{Box}(E_\gamma|E_N)$. The box distribution of photons is flat, with a height that scales as $\sim 1/E_N$ such that the difference between the height of two bins of the histogram is given by

$$\Delta N_\gamma \approx \lambda P_{\mathrm{vis}}(\lambda,\ell) \times \Delta E_\gamma \times \frac{\Phi_N(E_N = E_\gamma)}{E_\gamma}. \quad (15)$$

For $\lambda \gg \ell$, as in Fig. 8, $P_{\mathrm{vis}} \approx \ell/\lambda$ and the overall rate is independent of λ as discussed above. For $\lambda \sim \ell$, however, the probability of decaying inside the detector becomes some $O(1)$ number $P_{\mathrm{vis}} \approx 1 - \exp[-\ell/\lambda]$ and the photon spectrum becomes proportional to λ. Since $\lambda \propto E_N \propto E_\gamma$, this cancels against the $1/E_\gamma$ denominator of Eq. (15), and the spectrum for shorter decay lengths inherits the shape of Φ_N which is relatively flat for sub-GeV energies; this explains the shape of Fig. 9.

While our code is able to estimate the distribution of photons within Super-K, we only provide results from a rate-only analysis. A full analysis including the angular and spectral distributions of the decay photons would require considerations such as energetic and angular reconstruction of photon events in the detector, which are beyond the scope of this paper. We encourage those who have strong familiarity with Super-K to perform a more detailed analysis to improve constraints on new physics couplings.

We now consider future prospects and specifically upcoming experiments with larger fiducial volumes and

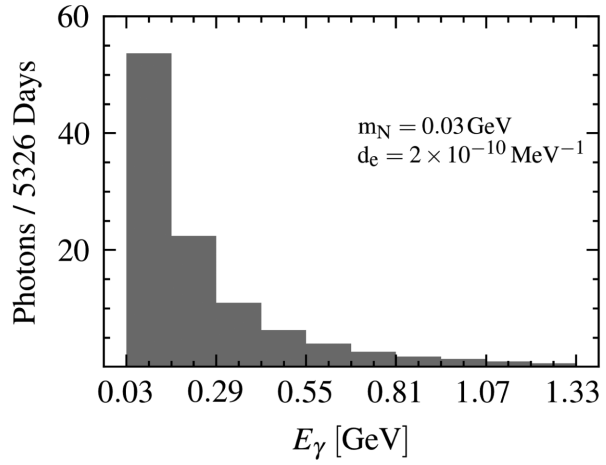

FIG. 8. Energy distribution of the detected photons for point A in Fig. 5 ($m_N = 0.03$ GeV and $d = 2 \times 10^{-10}$ MeV^{-1}). At low masses and small dipole couplings, the energy spectrum is IR peaked. The binning in E_γ is chosen to correspond to the binning in Super-Kamiokande's analysis of the sub-GeV atmospheric neutrino event sample [82].

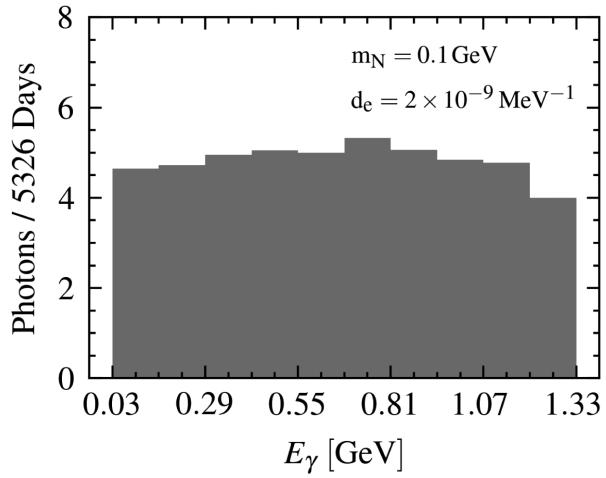

FIG. 9. Energy distribution of the detected photons for point B in Fig. 5 ($m_N = 0.1$ GeV and $d = 2 \times 10^{-9}$ MeV^{-1}). At larger masses and stronger dipole couplings, the energy spectrum is relatively flat. The binning in E_γ is chosen to correspond to the binning in Super-Kamiokande's analysis of the sub-GeV atmospheric neutrino event sample [82].

stronger background rejection methods. We consider Hyper-K, DUNE, and JUNO, all with 10 years of live time. We assume that the $\frac{\text{Atm Rate}}{\text{Fiducial volume}}$ for all three of these experiments is the same as Super-K. We also assume that the energy range of interest will be the same as Super-Kamiokande (30 MeV–1.33 GeV). When possible, we will consider an angular cut, meaning that we will only look at upward-going events. For Super-K, the Monte Carlo predicts 51% of the e-like 0-decay-e events to be down-going, while 49% are up-going [81]. We assume this holds for all experiments.

For 10 years at Hyper-K, we expect roughly 70,000 sub-GeV *e*-like 0-decay-e atmospheric events. Super-Kamiokande run IV is already doped with gadolinium and data from this exposure will have lower backgrounds from atmospheric neutrinos due to high-efficiency neutron tagging [85,86]. In our projections, we assume that Hyper-Kamiokande will be doped with gadolinium, which will cut the background from atmospheric neutrinos roughly in half. An angular cut will let us cut another ∼50% of the background, leaving us with roughly 17,000 background events. Assuming no systematic uncertainty, a 95%-C.L. bound can be set with 218 HNL events. This is, however, not likely to be realistic. The background uncertainties at Hyper-Kamiokande suffer from the same issues as at Super-Kamiokande where statistics are already high enough that a 5% systematic uncertainty makes the search entirely systematics limited. The increased statistical sample will not be helpful unless the systematic uncertainty on the Monte Carlo prediction can be brought down to subpercent levels even after accounting for reduced background rates from neutron tagging.

We expect roughly 9000 atmospheric events in a "sub-GeV sample" at DUNE over a 10 year run time. Since DUNE is a liquid-argon time projection chamber, it will be easier to distinguish the HNL decay products from a neutrino interaction. In particular, LArTPC technology offers (i) the ability to statistically discriminate between electrons and photons using measurements of $\mathrm{d}E/\mathrm{d}x$ at the beginning of a track, (ii) MeV-scale reconstruction capabilities that can tag gamma rays from nuclear deexcitations [87], and (iii) the ability to measure final state charged hadrons including protons, pions with kinetic energies above ∼10 MeV [88]. Finally, recent work has demonstrated that neutron tagging, using "sprays," may also be possible [89]. Importantly, for our background tagging purposes we only need to veto nuclear scattering events and/or single electron showers which is a much easier task than the energy reconstruction considered in [89]. While the ultimate capabilities of DUNE will require detailed simulation, we estimate that requiring upward-going events will cut 50% of the background, that proton tagging will catch 80% of the remaining events, and that searches for neutron sprays and associated gamma rays from nuclear deexcitation can cut out 80% of the remaining events for which no final state proton is produced. A naive combination of these estimates then suggests that 98% of the background could be rejected at DUNE, however, as we have already mentioned above, the precise value will require dedicated simulations. Performing an angular cut as well (requiring an up-going shower), we would expect a background of 88 events. With zero systematic uncertainty, 18 HNL events would set a 95%-C.L. bound, and this conclusion remains unchanged even if we allow for a ∼5% systematic on the background uncertainty. Note that, unlike SK, DUNE will be statistically limited provided it can achieve background rejections that are better than ∼90%.

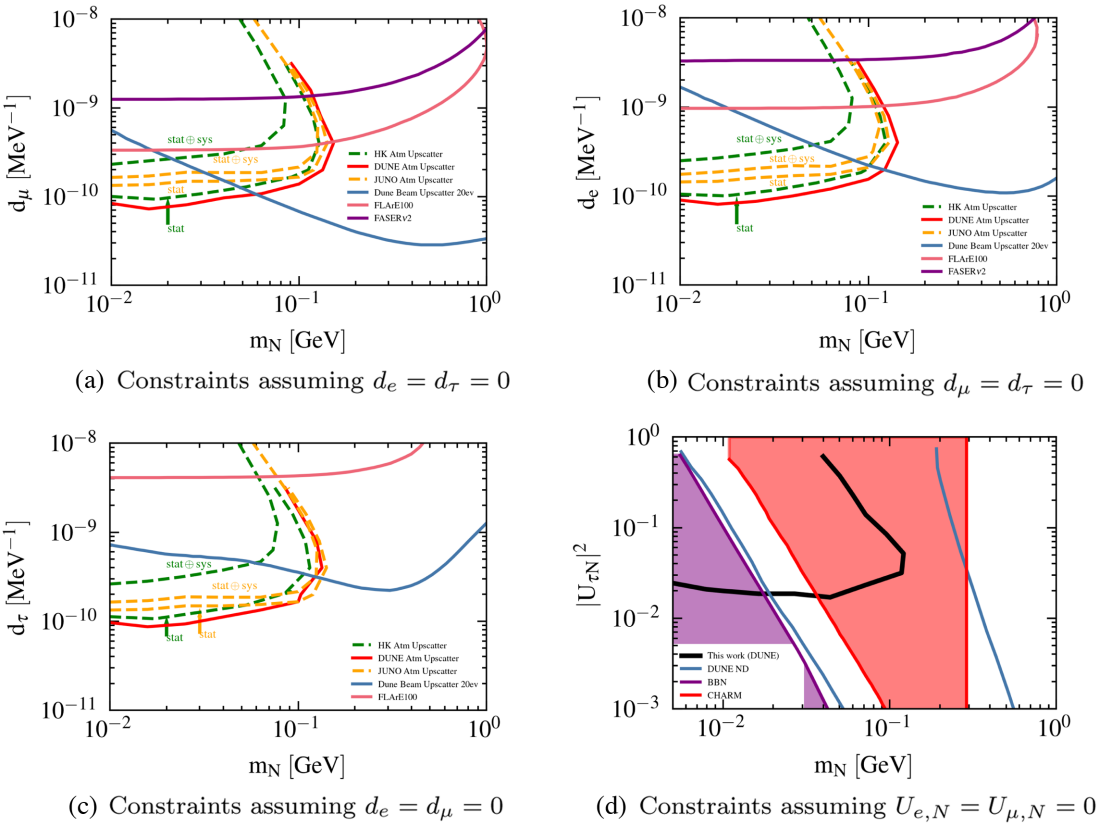

(a) Constraints assuming $d_e = d_\tau = 0$

(b) Constraints assuming $d_\mu = d_\tau = 0$

(c) Constraints assuming $d_e = d_\mu = 0$

(d) Constraints assuming $U_{e,N} = U_{\mu,N} = 0$

FIG. 10. Comparison of our projections for future dipole-portal and mass-mixing-portal limits vs other projections derived in the literature for (a) a muon-only dipole portal, (b) an electron-only dipole portal, (c) a tau-only dipole portal, and (d) a tau-only mass mixing portal. The parameter space probed by atmospheric up-scattering is already strongly excluded for electron-only and muon-only mass mixing portals are already excluded by existing data. Constraints from FLArE 100 and FASERν2 were derived in [51], and solar DUNE beam upscattering events were derived in [42]. We have included on Hyper-Kamiokande and JUNO for when $\sigma_{\rm sys} = 0$ and when $\sigma_{\rm sys}$ is 5% of the projected background. For our DUNE projection, the background was so low that the two bounds were nearly identical, so we only included the $\sigma_{\rm sys} = 0$ curve. For the mass-mixing constraints, we use current bounds from [47,64,66–69], along with a projected bound for a multipurpose DUNE near detector from [26].

Finally, for JUNO, we estimate roughly 6500 atmospheric events over 10 years. We expect that JUNO will be able to effectively cut out background from events that eject a proton due its low ~1 MeV detection threshold and will have a 50% efficiency at cutting background events that eject a neutron by leveraging the 2.2 MeV gamma ray from $np \to d\gamma$ [90]. Using the relative distributions of neutrinos and antineutrinos, we estimate that 20% of the atmospheric events will not produce a free proton and will instead produce a free neutron [91]. Assuming a $\gtrsim$95% efficiency at tagging protons, we therefore estimate that the background from atmospheric neutrino charged-current quasi-elastic will be ~10% of our rescaled background from SK, i.e., ~650 events. At these levels of statistics JUNO's statistical and assumed systematic uncertainties, taken again as 5%, are comparable.

For our projected limits on $|U_{\tau N}|^2$, we consider a 10 year period at DUNE. As mentioned before, we expect to have significant background reduction by rejecting events that have evidence of scattering off of a nucleon. As a benchmark, we take 30 BSM events in 10 years at DUNE to be statistically significant, and we show this contour in Fig. 10(d). We see that the projected constraint from a multipurpose near detector at DUNE [26] is quite close to constraints stemming from big bang nucleosynthesis [see Fig. 10(d)]. These two constraints contain much of the parameter space that would be probed by our projected atmospheric upscattering method, and so while we expect improved sensitivity it is likely that the DUNE near detector can cover most of the relevant parameter space. It would be interesting for future studies to identify near-term experiments that may be able to supply new constraints using existing datasets by leveraging atmospheric upscattering.

V. CONCLUSIONS

Atmospheric neutrinos have already given us a wealth of information regarding the nature of neutrino oscillation physics. Here we have seen that atmospheric neutrinos also provide a powerful and qualitatively distinct window into the nature of neutrino interactions and heavy sterile

neutrinos. In particular, we have examined the upscattering of atmospheric neutrinos to HNLs and their subsequent decay inside of terrestrial detectors, finding that current data from Super-Kamiokande already yield leading constraints on both the dipole and mass-mixing portals. For the dipole portal, these bounds eat into new parameter space for HNL masses around $10 \lesssim m_N \lesssim 100$ MeV, with precise constraints depending on which active neutrino flavor coupling dominates. Similarly, for the mass-mixing portal our Super-Kamiokande constraints provide leading constraints on the tau-sterile mixing angle for HNLs around ∼20 MeV.

In the near future, experiments such as DUNE, Hyper-Kamiokande, and JUNO will be able to take advantage of improved particle identification and background rejection and employ dedicated search strategies incorporating angular distribution of the events to improve the bounds on the dipole couplings by around a factor of ∼2.5 at low HNL masses. As such, this search strategy nicely complements the DUNE beam upscattering [42] and double bang searches [47] which provide better sensitivity to higher HNLs masses, $m_N \gtrsim 100$ MeV on the dipole-portal coupling, and HNLs produced from meson decays at DUNE for the mass-mixing portal [76]. As an illustration of the strength of the future bounds, it is striking to observe that JUNO, Hyper-K, and DUNE appear poised to overlap in coupling reach with SN1987A [35] and will therefore close off an allowed gap in couplings.

ACKNOWLEDGMENTS

We thank Volodymyr Takhistov for comments on our manuscript and for useful discussions regarding the classification of single photons in SK. R. P. thanks Patrick Fox for comments on our manuscript and for helpful discussions regarding the numerical implementation of the upscattering volume integral, as well as Pedro Machado for comments on our manuscript and for discussion on atmospheric neutrino backgrounds in Super-Kamiokande and DUNE. We also thank Carlos Argüelles for helpful discussions and feedback. This work was supported by the U.S. Department of Energy, Office of Science, Office of High Energy Physics, under Awards No. DE-SC0019095 and No. DE-SC002025. This manuscript has been authored by Fermi Research Alliance, LLC under Contract No. DE-AC02-07CH11359 with the U.S. Department of Energy, Office of Science, Office of High Energy Physics. This research was performed at the Kavli Institute for Theoretical Physics which is supported in part by the National Science Foundation under Grant No. NSF PHY-1748958 and at the Aspen Center for Physics, which is supported by National Science Foundation Grant No. PHY-1607611.

APPENDIX A: MONTE CARLO ROUTINE

1. Sampling values

The Monte Carlo routine begins by sampling a neutrino energy E_ν. We want our distribution of energies to follow a power spectrum, since both the flux of atmospheric neutrinos and the scattering cross section follow a power law with respect to energy. We consider a maximum (minimum) energy $E_{\nu,\max}(E_{\nu,\min})$,

$$\rho_E = \kappa E_\nu^{-\gamma}, \tag{A1}$$

$$\kappa = \frac{1-\gamma}{E_{\nu,\max}^{1-\gamma} - E_{\nu,\min}^{1-\gamma}}. \tag{A2}$$

To get our energy, we uniformly sample a number $\chi \in [0,1]$ and then

$$E_\nu = \left(\frac{1-\gamma}{\kappa}\chi + (E_{\nu,\min})^{1-\gamma}\right)^{\frac{1}{1-\gamma}}. \tag{A3}$$

To sample the position of interaction, we want a distribution that mimics the decay length of the HNL. We define our minimum desired distance from the detector as $R_{\min}$, and the maximum distance $R_{\max} = R_\oplus + |\mathbf{Y}|$. Then,

$$r' = R_{\min} - \lambda \ln(1 - \chi[1 - e^{\frac{\Delta R}{\lambda}}]), \tag{A4}$$

with $\Delta R = R_{\min} - R_{\max}$, and $\chi \in [0,1]$. We then sample ϕ' uniformly and sample $\cos\theta'$ uniformly from angles that leave the interaction within Earth. Then, the interaction location is

$$\mathbf{X} = \mathbf{Y} + (r'\sin\theta'\cos\phi', r'\sin\theta'\sin\phi', r'\cos\theta'). \tag{A5}$$

If $\mathbf{X} > R_\oplus$, we reject and repeat the sampling until we get an interaction position within Earth.

For sampling the scattering angles, we note that some models favor forward scattering, while others have scattering cross sections that have quasiuniform angular distributions. We define a minimum (maximum) scattering angle $\Theta_{\min}$ ($\Theta_{\max}$) based on allowed kinematics, and a value of $\epsilon \in \{0,1\}$ based on the type of scattering

$$\rho_\Theta = \beta(1-\cos\Theta)^{-\epsilon}, \tag{A6}$$

so that for $\epsilon = 1$ we have

$$\beta = [\ln((1-\cos\Theta_{\max})/(1-\cos\Theta_{\min}))]^{-1}, \tag{A7}$$

while for $\epsilon = 0$ we have

$$\beta = [\cos\Theta_{\min} - \cos\Theta_{\max}]^{-1}. \tag{A8}$$

For sampling the scattering angle, we sample a uniform number $\chi \in [0,1]$, such that the angles are sampled as

$$\cos\Theta = 1 - (1-\cos\Theta_{\max})^{\chi}(1-\cos\Theta_{\min})^{1-\chi}, \tag{A9}$$

$$\cos\Theta = \cos\Theta_{\max} + \chi(\cos\Theta_{\min} - \cos\Theta_{\max}), \tag{A10}$$

for $\epsilon = 1$ and $\epsilon = 0$ respectively.

Finally, we want to sample the neutrino entry position $\mathbf{W}$. We define $\mathbf{v}_{\rm in} = \mathbf{X} - \mathbf{W}$. Using our scattering angle Θ that we sampled and another angle ψ uniformly sampled from 0 to 2π, then

$$\hat{\mathbf{v}}_{\rm in} = \frac{\mathbf{Y}-\mathbf{X}}{|\mathbf{Y}-\mathbf{X}|}\cos\Theta + \hat{\mathbf{v}}_{\mathbf{1}\perp}\sin\Theta\cos\psi + \hat{\mathbf{v}}_{\mathbf{2}\perp}\sin\Theta\sin\psi, \tag{A11}$$

where $\mathbf{Y}-\mathbf{X}$, $\mathbf{v}_{\mathbf{1}\perp}$, and $\mathbf{v}_{\mathbf{2}\perp}$ are all mutually orthogonal. To find the length of the path traveled, we use

$$|\mathbf{v_{in}}| = \mathbf{X}\cdot\hat{\mathbf{v}}_{\mathbf{in}} + \sqrt{(\mathbf{X}\cdot\hat{\mathbf{v}}_{\mathbf{in}})^2 + R_\oplus^2 - |\mathbf{X}|^2}. \tag{A12}$$

Finally, we get $\mathbf{W} = \mathbf{X} - \hat{\mathbf{v}}_{\mathbf{in}}|\mathbf{v_{in}}|$.

2. Calculations

Having sampled our energy, scattering angle, interaction position, and neutrino entry position, we can calculate other necessary values. From $\mathbf{W}$ and $\mathbf{X}$, we calculate the zenith angle $\phi_{\rm zen}$ of the incoming neutrinos (Fig. 1). We use NuFlux [74] to calculate $\mathcal{I}_{\rm incoming}(E_\nu, \phi_{\rm zen})$. When working with flavor-dependent couplings, we calculate a 1D density profile from $\mathbf{W}$ to $\mathbf{X}$ using the preliminary Earth reference model (PREM) [92]. Oscillations are calculated by integrating along this density profile to obtain $I_{\nu_\alpha}(E_\nu, \phi_{\rm zen}, \mathbf{X})$.

At $\mathbf{X}$, we use the PREM [92] to calculate the density and call a saved dictionary of the number density for each of the elements [93,94]. We calculate the cross sections for the scattering using methods described in Appendix B to get $\sum_A n_A \frac{d\sigma_A}{d\cos\Theta} = (n\frac{d\sigma}{d\cos\Theta})_{\rm eff}$. We calculate the decay length of the HNL using Eq. (5) and probability for producing a visible decay from Eq. (6).

3. Weighting

Since we preferentially sample our values, we must include a weighting when calculating the rate of decays from the Monte Carlo. These weights are calculated by taking the ratio of our sampling distribution to the true integrand. Explicitly, the weights are given by

$$\begin{aligned} w_E(E_{\nu,i}) &= \frac{(E_{\nu,i})^\gamma}{\kappa(E_{\nu,\max}-E_{\nu,\min})}, \\ w_\Theta(\Theta_i) &= \frac{1}{\beta}\frac{(1-\cos\Theta_i)^\epsilon}{\cos(\Theta_{\min})-\cos(\Theta_{\max})}, \\ w_V(\lambda_i, r_i') &= \frac{e^{r_i'/\lambda}[e^{-R_{\min}/\lambda_i} - e^{-R_{\max}/\lambda_i}]}{(R_{\max}-R_{\min})V_\oplus}\frac{dV}{dR}R_{\max}, \end{aligned} \tag{A13}$$

where

$$\frac{dV}{dR} = \begin{cases} \frac{4\pi}{3}(r')^2 & \text{if } R_\oplus > |\mathbf{Y}| + r' \\ \frac{\pi r'}{|\mathbf{Y}|}(R_\oplus^2 - [|\mathbf{Y}| - r']^2) & \text{else.} \end{cases} \tag{A14}$$

In a Monte Carlo without preferential sampling, we would have standard "Riemann weights," $\Delta\mathbf{X}\Delta E_\nu \Delta\cos\Theta/N$ with $\Delta\mathbf{X} = V_\oplus$, $\Delta E_\nu = (E_{\nu,\max} - E_{\nu,\min})$, $\Delta\cos\Theta = (\cos(\Theta_{\min}) - \cos(\Theta_{\max}))$, and N the number of samples in our Monte Carlo. Notice that upon combination (multiplying all weights together) the denominators in our new sampling weights, Eq. (A13), cancel against the uniform weights such that we obtain the weight for the ith sample as

$$w_i = \frac{V_\oplus (E_{\nu,i})^\gamma (1-\cos\Theta_i)^\epsilon}{\kappa\beta N} w_V(\lambda_i, r_i'). \tag{A15}$$

We now have everything needed to compute the rate

$$R = \sum_{i=1}^{N}\left(n\frac{d\sigma}{d\cos\Theta}\right)_{\rm eff} \times \mathcal{I}_\nu \times \frac{P_{\rm vis}}{4\pi|\mathbf{X}-\mathbf{Y}|^2} w_i. \tag{A16}$$

This is the numerical cousin of Eq. (7). In this routine, between 20,000 and 300,000 events were generated for each simulation. The larger simulations were necessary for the mass-mixing model.

APPENDIX B: UPSCATTERING CROSS SECTIONS

1. Dipole portal

For dipole upscattering, the cross section can be decomposed into

$$\frac{d\sigma}{dt} = \frac{d\sigma_{\rm coh}}{dt}|F(-t)|^2 + \frac{d\sigma_{\rm p}}{dt}Z(1-|F(-t)|^2) + \frac{d\sigma_{\rm n}}{dt}(A-Z), \tag{B1}$$

where A and Z are the atomic mass and atomic number of the nucleus respectively and $F(-t)$ is the form factor for the transferred momentum. We work in the infinite mass limit, so our transferred momentum goes as

$$t_{\rm coh} = 2E_\nu^2 - m_N^2 - 2E_\nu\sqrt{E_\nu^2 - m_N^2}\cos\Theta. \tag{B2}$$

The coherent scattering is given in Eq. (9) with $\mathbf{Q}^2 = -t$. Meanwhile, incoherent scattering off of protons or neutrons will go as

$$\begin{aligned} \frac{d\sigma_{\rm in}}{dt} = &\frac{\alpha d^2(m_N^2 t - 2m_N^4 + t^2)}{m_p^2 t^2 (m_p^2 - s)^2} \\ &\times [2F_1^2 m_p^2(2m_p^2 + t) - 12F_1F_2m_p^2 t + F_2^2 t(8m_p^2 + t)]. \end{aligned} \tag{B3}$$

Here, m_p is the mass of a nucleon, and s is the center-of-mass energy given by $m_p^2 + 2m_p E_\nu$. The value of t for incoherent scattering goes as

$$t_{\text{in}} = m_N^2 - 2E_\nu\left(E_N - \sqrt{E_N^2 - m_N^2}\cos\Theta\right). \quad \text{(B4)}$$

If the neutrino scatters incoherently, then the energy of the HNL is

$$E_{N\text{incoh}} = \frac{(E_\nu + m_p)(m_N^2 + 2E_\nu m_p)}{2(E_\nu^2\sin^2\Theta + 2E_\nu m_p + m_p^2)} + \frac{E_\nu\cos\Theta\sqrt{-4m_N^2(m_p^2 + E_\nu^2\sin^2\Theta) + m_N^2 - 2E_\nu m_p^2}}{2(E_\nu^2\sin^2\Theta + 2E_\nu m_p + m_p^2)}. \quad \text{(B5)}$$

Finally, we need to calculate the F_1 and F_2 values [95,96]

$$F_{1,p/n} = \frac{1}{1 - \frac{Q^2}{4m_p^2}}\left(G_E^{p/n} + \frac{Q^2}{4m_p^2}\times G_M^{p/n}\right),$$
$$F_{2,p/n} = \frac{1}{1 - \frac{Q^2}{4m_p^2}}(G_M^{p/n} - G_E^{p/n}), \quad \text{(B6)}$$

where

$$G_E^p = G_D,$$
$$G_E^n = 0,$$
$$G_M^{p,n} = \mu_{p,n}G_D,$$
$$G_D = \left(1 + \frac{Q^2}{0.71\ \text{GeV}^2}\right)^{-2}, \quad \text{(B7)}$$

and $\mu_p = 2.793$, $\mu_n = -1.913$, and $Q^2 = t$.

In our routine, while we use Eqs. (B2) and (B4) for finding the transferred momentum, we do not know if the true scattering is coherent or incoherent [Eq. (B1) says that we have components of both]. Therefore, we let the energy of the propagating HNL be E_ν.

When implementing the full cross section, we find that the coherent part still dominates, so most of our phenomenology can be explained by considering the coherent case.

2. Mass-mixing routine

In the mass-mixing portal, we must consider coherent elastic scattering, incoherent scattering on nucleons, and deep-inelastic scattering (DIS). Unlike the dipole portal, where nearly all scattering is coherent, the mass-mixing model has significant contributions from incoherent scattering. Since different forms of scattering lead to different HNL energies (and therefore different observed energies), we run the simulations independently for each type of scattering and then sum together the rates to get the total contribution.

For coherent scattering, we have

$$\frac{d\sigma_{\text{coh}}}{dt} = \frac{|U_{\alpha N}|^2 G_F^2 Q_w^2}{2\pi}\left(1 - \frac{m_N^2}{4E_\nu^2} + \frac{t}{4E_\nu^2}\right)|F(-t)|^2. \quad \text{(B8)}$$

In Eq. (B8), G_F is the Fermi coupling constant and Q_w is the weak charge of the nucleus.

Incoherent scattering is modeled by treating nuclei as collections of free nucleons and using standard hadronic form factors for the nuclei. We take dipole parametrizations of the vector, magnetic, and axial form factors and rely on a partially conserved axial current ansatz for the pseudoscalar form factor; explicit expressions can be found in [97,98].

For DIS, we consider scattering off of individual quarks. To find the cross section, we first find the cross section for scattering off of quarks σ_f as a function of the momentum carried by the quark. This is parametrized by x, the fraction of the total longitudinal nucleon momentum carried by the quark. Finally, we have

$$\sigma_{\text{DIS}} = \int_0^1\left(\sum_f \sigma_f(x) f_f(x)\right)dx, \quad \text{(B9)}$$

where $f_f(x)$ is the parton distribution function (PDF) for the particular quark.

We numerically performed the integral in Eq. (B9), using PDFs from [99] and treating the HNL as massless, since the masses we are sensitive to are far below the GeV energy scale where DIS becomes important. Although the cross section for DIS scales linearly with neutrino energy, the DIS only contributes on the order of a few percent in the region of parameter space that is not covered by existing searches. Therefore, in our code, we use a simple form for DIS with the leading coefficient determined by Eq. (B9),

$$\frac{d\sigma_{\text{DIS}}}{d\cos\Theta} = \frac{|U_{\alpha N}|^2 E_\nu}{2}\sqrt{1 - \frac{m_N^2}{s}} \times (1 - |F(-t)|^2) \times 3 \times 10^{-39}\ \text{cm}^2. \quad \text{(B10)}$$

From these scattering channels, we can determine the number of visible decays (in this case, $N \to \nu e^+ e^-$) expected for Super-K. We assume that Super-Kamiokande will be unable to resolve both the e^+ and the e^-, so the decay will appear as a sub-GeV 0-decay-e event. We calculate the energy of the e^+e^- pair by using the invariant mass distribution in [100] and require that the energy be between 30 MeV and 1.33 GeV. We see the resulting bounds in Fig. 2(d).

3. Form factor fitting

We can see that for Eq. (B1), we need a way to calculate the nuclear form factor. The Helm form factor allows us to accomplish this

$$F_{\mathrm{Helm}}(Q^2) = \left(\frac{3j_1(QR_1)}{QR_1}\right)^{1/2} \times \mathrm{e}^{-(sQ)^2/2}, \tag{B11}$$

where j_1 is a spherical Bessel function of the first kind and

$$R_1 = \sqrt{R_A^2 + \frac{7\pi^2}{3}r_0^2 - 5s^2}. \tag{B12}$$

Rather than using default parameters as a global description of all nuclei, we fit the values of R_A, r_0, and s independently for each nucleus, and then store these values for later calculation. We begin by taking the two-parameter Fermi distribution for the radial nuclear charge distribution from [75]. Taking the 3D Fourier transform of this charge distribution gives us the charge form factor. Using initial values of R_A, r_0, and s, we define the difference between the Fermi and Helm form factors as

$$S = \sum_i (F^2_{\mathrm{Helm}}(Q_i^2, R_A, r_0, s) - F^2_{\mathrm{Fermi}}(Q_i^2))^2. \tag{B13}$$

We then use gradient ascent to iteratively improve our fit [i.e., $R_1 \to R_1 - (\mathrm{d}S/\mathrm{d}R_1)\delta R_1$ where δR_1 is some predetermined constant].

APPENDIX C: EARTH MODEL

To find the local density of Earth $\rho(X)$ at the location of neutrino interaction, we use the preliminary reference Earth model, specifically Table IV of [92].

TABLE I. Fractional weights for elements in each layer of Earth.

Element	Crust (%)	Mantle (%)	Core (%)
O	46.6	44	0
Si	27.72	21	6
Al	8.13	2.35	0
Fe	5.05	6.26	85.5
Ca	3.65	2.5	0
Na	2.75	0	0
K	2.58	0	0
Mg	2.08	22.8	0
S	0	0	1.9
Ni	0	0	5.2
Total	98.56	98.91	98.6

We need to determine the number density of each element at the interaction location. To do this, we obtain the elemental weight fraction of the core and mantle from [93] and the crust weight fractions from [94]. The results are summarized in Table I.

We can now calculate the number density of each element n_i by

$$n_i(\mathbf{X}) = \frac{\rho(\mathbf{X})f_i}{m_i} \times N_A, \tag{C1}$$

where N_A is Avagadro's number, and f_i and m_i are the fractional weight and molar mass of the element in question, respectively.

[1] Brian Patt and Frank Wilczek, Higgs-field portal into hidden sectors, arXiv:hep-ph/0605188.

[2] Brian Batell, Maxim Pospelov, and Adam Ritz, Exploring portals to a hidden sector through fixed targets, Phys. Rev. D **80**, 095024 (2009).

[3] J. Beacham *et al.*, Physics beyond colliders at CERN: Beyond the standard model working group report, J. Phys. G **47**, 010501 (2020).

[4] Prateek Agrawal *et al.*, Feebly-interacting particles: FIPs 2020 workshop report, Eur. Phys. J. C **81**, 1015 (2021).

[5] Luis Alvarez-Gaume and Edward Witten, Gravitational anomalies, Nucl. Phys. **B234**, 269 (1984).

[6] J. C. Montero and V. Pleitez, Gauging U(1) symmetries and the number of right-handed neutrinos, Phys. Lett. B **675**, 64 (2009).

[7] Harald Fritzsch and Peter Minkowski, Unified interactions of leptons and hadrons, Ann. Phys. (N.Y.) **93**, 193 (1975).

[8] K. S. Babu, Model of, Calculable Majorana neutrino masses, Phys. Lett. B **203**, 132 (1988).

[9] A. Zee, Quantum numbers of Majorana neutrino masses, Nucl. Phys. **B264**, 99 (1986).

[10] Juan Herrero-Garcia, Miguel Nebot, Nuria Rius, and Arcadi Santamaria, The Zee–Babu model revisited in the light of new data, Nucl. Phys. **B885**, 542 (2014).

[11] Peter Minkowski, $\mu \to e\gamma$ at a rate of one out of 10^9 muon decays? Phys. Lett. **67B**, 421 (1977).

[12] Tsutomu Yanagida, Horizontal gauge symmetry and masses of neutrinos, Conf. Proc. C **7902131**, 95 (1979).

[13] Murray Gell-Mann, Pierre Ramond, and Richard Slansky, Complex spinors and unified theories, Conf. Proc. C **790927**, 315 (1979).
[14] Carlos Argüelles, Pilar Coloma, Pilar Hernández, and Víctor Muñoz, Searches for atmospheric long-lived particles, J. High Energy Phys. 02 (2020) 190.
[15] D. Liventsev *et al.* (Belle Collaboration), Search for heavy neutrinos at Belle, Phys. Rev. D **87**, 071102 (2013); Erratum, Phys. Rev. D **95**, 099903 (2017).
[16] Takehiko Asaka and Mikhail Shaposhnikov, The νMSM, dark matter and baryon asymmetry of the universe, Phys. Lett. B **620**, 17 (2005).
[17] Takehiko Asaka, Steve Blanchet, and Mikhail Shaposhnikov, The nuMSM, dark matter and neutrino masses, Phys. Lett. B **631**, 151 (2005).
[18] Anupama Atre, Tao Han, Silvia Pascoli, and Bin Zhang, The search for heavy Majorana neutrinos, J. High Energy Phys. 05 (2009) 030.
[19] Loretta M. Johnson, Douglas W. McKay, and Tim Bolton, Extending sensitivity for low mass neutral heavy lepton searches, Phys. Rev. D **56**, 2970 (1997).
[20] Jean-Michel Levy (T2K Collaboration), Rates and differential distributions in heavy neutral leptons production and decays, arXiv:1805.06419.
[21] Joseph A. Formaggio, Janet M. Conrad, Michael Shaevitz, Artur Vaitaitis, and Robert Drucker, Helicity effects in neutral heavy lepton decays, Phys. Rev. D **57**, 7037 (1998).
[22] Dmitry Gorbunov and Mikhail Shaposhnikov, How to find neutral leptons of the νMSM? J. High Energy Phys. 10 (2007) 015; Erratum, J. High Energy Phys. 11 (2013) 101.
[23] Marco Drewes, The phenomenology of right handed neutrinos, Int. J. Mod. Phys. E **22**, 1330019 (2013).
[24] Kyrylo Bondarenko, Alexey Boyarsky, Dmitry Gorbunov, and Oleg Ruchayskiy, Phenomenology of GeV-scale heavy neutral leptons, J. High Energy Phys. 11 (2018) 032.
[25] Alexey Boyarsky, Oleg Ruchayskiy, and Mikhail Shaposhnikov, The role of sterile neutrinos in cosmology and astrophysics, Annu. Rev. Nucl. Part. Sci. **59**, 191 (2009).
[26] Jeffrey M. Berryman, Andre de Gouvea, Patrick J. Fox, Boris Jules Kayser, Kevin James Kelly, and Jennifer Lynne Raaf, Searches for decays of new particles in the DUNE multi-purpose near detector, J. High Energy Phys. 02 (2020) 174.
[27] Peter Ballett, Tommaso Boschi, and Silvia Pascoli, Heavy neutral leptons from low-scale seesaws at the DUNE near detector, J. High Energy Phys. 03 (2020) 111.
[28] Graciela B. Gelmini, Alexander Kusenko, and Volodymyr Takhistov, Possible hints of sterile neutrinos in recent measurements of the hubble parameter, J. Cosmol. Astropart. Phys. 06 (2021) 002.
[29] S. N. Gninenko, The MiniBooNE Anomaly and Heavy Neutrino Decay, Phys. Rev. Lett. **103**, 241802 (2009).
[30] Sergei N. Gninenko, A resolution of puzzles from the LSND, KARMEN, and MiniBooNE experiments, Phys. Rev. D **83**, 015015 (2011).
[31] David McKeen and Maxim Pospelov, Muon capture constraints on sterile neutrino properties, Phys. Rev. D **82**, 113018 (2010).
[32] Manuel Masip and Pere Masjuan, Heavy-neutrino decays at neutrino telescopes, Phys. Rev. D **83**, 091301 (2011).
[33] Manuel Masip, Pere Masjuan, and Davide Meloni, Heavy neutrino decays at MiniBooNE, J. High Energy Phys. 01 (2013) 106.
[34] Pilar Coloma, Pedro A. N. Machado, Ivan Martinez-Soler, and Ian M. Shoemaker, Double-Cascade Events from New Physics in IceCube, Phys. Rev. Lett. **119**, 201804 (2017).
[35] Gabriel Magill, Ryan Plestid, Maxim Pospelov, and Yu-Dai Tsai, Dipole portal to heavy neutral leptons, Phys. Rev. D **98**, 115015 (2018).
[36] Vedran Brdar, Admir Greljo, Joachim Kopp, and Toby Opferkuch, The neutrino magnetic moment portal: Cosmology, astrophysics, and direct detection, J. Cosmol. Astropart. Phys. 01 (2021) 039.
[37] Ian M. Shoemaker and Jason Wyenberg, Direct detection experiments at the neutrino dipole portal frontier, Phys. Rev. D **99**, 075010 (2019).
[38] Carlos A. Argüelles, Matheus Hostert, and Yu-Dai Tsai, Testing New Physics Explanations of the MiniBooNE Anomaly at Neutrino Scattering Experiments, Phys. Rev. Lett. **123**, 261801 (2019).
[39] Matheus. Hostert, Hidden physics at the neutrino frontier: Tridents, dark forces, and hidden particles, Ph.D. thesis, Durham University, 2019.
[40] Oliver Fischer, Álvaro Hernández-Cabezudo, and Thomas Schwetz, Explaining the MiniBooNE excess by a decaying sterile neutrino with mass in the 250 MeV range, Phys. Rev. D **101**, 075045 (2020).
[41] Pilar Coloma, Pilar Hernández, Víctor Muñoz, and Ian M. Shoemaker, New constraints on Heavy Neutral Leptons from Super-Kamiokande data, Eur. Phys. J. C **80**, 235 (2020).
[42] Thomas Schwetz, Albert Zhou, and Jing-Yu Zhu, Constraining active-sterile neutrino transition magnetic moments at DUNE near and far detectors, J. High Energy Phys. 07 (2021) 200.
[43] Chiara Arina, Andrew Cheek, Ken Mimasu, and Luca Pagani, Light and darkness: Consistently coupling dark matter to photons via effective operators, Eur. Phys. J. C **81**, 223 (2021).
[44] Ian M. Shoemaker, Yu-Dai Tsai, and Jason Wyenberg, Active-to-sterile neutrino dipole portal and the XENON1T excess, Phys. Rev. D **104**, 115026 (2021).
[45] Asli Abdullahi, Matheus Hostert, and Silvia Pascoli, A dark seesaw solution to low energy anomalies: MiniBooNE, the muon $(g-2)$, and *BABAR*, Phys. Lett. B **820**, 136531 (2021).
[46] Soroush Shakeri, Fazlollah Hajkarim, and She-Sheng Xue, Shedding new light on sterile neutrinos from XENON1T experiment, J. High Energy Phys. 12 (2020) 194.
[47] Mack Atkinson, Pilar Coloma, Ivan Martinez-Soler, Noemi Rocco, and Ian M. Shoemaker, Heavy neutrino searches through double-bang events at Super-Kamiokande, DUNE, and Hyper-Kamiokande, J. High Energy Phys. 04 (2022) 174.
[48] Wonsub Cho, Ki-Young Choi, and Osamu Seto, Sterile neutrino dark matter with dipole interaction, Phys. Rev. D **105**, 015016 (2022).
[49] Jihn E. Kim, Arnab Dasgupta, and Sin Kyu Kang, Probing neutrino dipole portal at COHERENT experiment, J. High Energy Phys. 11 (2021) 120.

[50] Carlos A. Argüelles, Nicolò Foppiani, and Matheus Hostert, Heavy neutral leptons below the kaon mass at hodoscopic detectors, Phys. Rev. D **105**, 095006 (2022).
[51] Ahmed Ismail, Sudip Jana, and Roshan Mammen Abraham, Neutrino up-scattering via the dipole portal at forward LHC detectors, Phys. Rev. D **105**, 055008 (2022).
[52] O. G. Miranda, D. K. Papoulias, O. Sanders, M. Tórtola, and J. W. F. Valle, Low-energy probes of sterile neutrino transition magnetic moments, J. High Energy Phys. 12 (2021) 191.
[53] Patrick D. Bolton, Frank F. Deppisch, Kåre Fridell, Julia Harz, Chandan Hati, and Suchita Kulkarni, Probing active-sterile neutrino transition magnetic moments with photon emission from CEνNS, Phys. Rev. D **106**, 035036 (2022).
[54] Krzysztof Jodłowski and Sebastian Trojanowski, Neutrino beam-dump experiment with FASER at the LHC, J. High Energy Phys. 05 (2021) 191.
[55] Stefano Vergani, Nicholas W. Kamp, Alejandro Diaz, Carlos A. Argüelles, Janet M. Conrad, Michael H. Shaevitz, and Melissa A. Uchida, Explaining the MiniBooNE excess through a mixed model of neutrino oscillation and decay, Phys. Rev. D **104**, 095005 (2021).
[56] D. Aristizabal Sierra, O. G. Miranda, D. K. Papoulias, and G. Sanchez Garcia, Neutrino magnetic and electric dipole moments: From measurements to parameter space, Phys. Rev. D **105**, 035027 (2022).
[57] A. Baha Balantekin, André de Gouvêa, and Boris Kayser, Addressing the Majorana vs Dirac question with neutrino decays, Phys. Lett. B **789**, 488 (2019).
[58] André de Gouvêa, Patrick J. Fox, Boris J. Kayser, and Kevin J. Kelly, Characterizing heavy neutral fermions via their decays, Phys. Rev. D **105**, 015019 (2022).
[59] K. S. Babu, Sudip Jana, Manfred Lindner, and Vishnu P. K, Muon $g-2$ anomaly and neutrino magnetic moments, J. High Energy Phys. 10 (2021) 240.
[60] Ryan Plestid, Luminous solar neutrinos I: Dipole portals, Phys. Rev. D **104**, 075027 (2021).
[61] Enrico Bertuzzo, Sudip Jana, Pedro A. N. Machado, and Renata Zukanovich Funchal, Dark Neutrino Portal to Explain MiniBooNE Excess, Phys. Rev. Lett. **121**, 241801 (2018).
[62] Peter Ballett, Matheus Hostert, and Silvia Pascoli, Dark neutrinos and a three portal connection to the Standard Model, Phys. Rev. D **101**, 115025 (2020).
[63] Peter Ballett, Matheus Hostert, and Silvia Pascoli, Neutrino masses from a dark neutrino sector below the electroweak scale, Phys. Rev. D **99**, 091701 (2019).
[64] Ryan Plestid, Luminous solar neutrinos II: Mass-mixing portals, Phys. Rev. D **104**, 075028 (2021).
[65] J. Altegoer *et al.* (NOMAD Collaboration), The NOMAD experiment at the CERN SPS, Nucl. Instrum. Methods Phys. Res., Sect. A **404**, 96 (1998).
[66] R. Acciarri, C. Adams, J. Asaadi, B. Baller, V. Basque, F. Cavanna, A. de Gouvêa, R. S. Fitzpatrick, B. Fleming, P. Green, C. James, K. J. Kelly, I. Lepetic, X. Luo, O. Palamara, G. Scanavini, M. Soderberg, J. Spitz, A. M. Szelc, W. Wu, and T. Yang (ArgoNeuT Collaboration), New Constraints on Tau-Coupled Heavy Neutral Leptons with Masses $m_N = 280$–970 MeV, Phys. Rev. Lett. **127**, 121801 (2021).
[67] J. Orloff, Alexandre N. Rozanov, and C. Santoni, Limits on the mixing of tau neutrino to heavy neutrinos, Phys. Lett. B **550**, 8 (2002).
[68] Iryna Boiarska, Alexey Boyarsky, Oleksii Mikulenko, and Maksym Ovchynnikov, Constraints from the CHARM experiment on heavy neutral leptons with tau mixing, Phys. Rev. D **104**, 095019 (2021).
[69] Nashwan Sabti, Andrii Magalich, and Anastasiia Filimonova, An extended analysis of heavy neutral leptons during big bang nucleosynthesis, J. Cosmol. Astropart. Phys. 11 (2020) 056.
[70] M. Honda, M. Sajjad Athar, T. Kajita, K. Kasahara, and S. Midorikawa, Atmospheric neutrino flux calculation using the NRLMSISE-00 atmospheric model, Phys. Rev. D **92**, 023004 (2015).
[71] Ivan Esteban, M. C. Gonzalez-Garcia, Michele Maltoni, Thomas Schwetz, and Albert Zhou, The fate of hints: Updated global analysis of three-flavor neutrino oscillations, J. High Energy Phys. 09 (2020) 178.
[72] Joshua Eby, Patrick J. Fox, Roni Harnik, and Graham D. Kribs, Luminous signals of inelastic dark matter in large detectors, J. High Energy Phys. 09 (2019) 115.
[73] Patrick Fox (private communication).
[74] The IceCube Collaboration, NuFlux: A library for calculating atmospheric neutrino fluxes (v2.0.3), Zenodo, 2022, 10.5281/zenodo.5874708.
[75] H. De Vries, C. W. De Jager, and C. De Vries, Nuclear charge and magnetization density distribution parameters from elastic electron scattering, At. Data Nucl. Data Tables **36**, 495 (1987).
[76] Pilar Coloma, Enrique Fernández-Martínez, Manuel González-López, Josu Hernández-García, and Zarko Pavlovic, GeV-scale neutrinos: Interactions with mesons and DUNE sensitivity, Eur. Phys. J. C **81**, 78 (2021).
[77] A. Baha Balantekin and Boris Kayser, On the properties of neutrinos, Annu. Rev. Nucl. Part. Sci. **68**, 313 (2018).
[78] Boris Kayser, *Proceedings of the 53rd Rencontres de Moriond on Electroweak Interactions and Unified Theories* (ARISF, 2018), pp. 323–326.
[79] Shyam Balaji, Maura Ramirez-Quezada, and Ye-Ling Zhou, *CP* violation and circular polarisation in neutrino radiative decay, J. High Energy Phys. 04 (2020) 178.
[80] K. Abe *et al.* (Super-Kamiokande Collaboration), Limits on sterile neutrino mixing using atmospheric neutrinos in Super-Kamiokande, Phys. Rev. D **91**, 052019 (2015).
[81] M. Jiang *et al.* (Super-Kamiokande Collaboration), Atmospheric neutrino oscillation analysis with improved event reconstruction in Super-Kamiokande IV, Prog. Theor. Exp. Phys. **2019**, 053F01 (2019).
[82] K. Abe *et al.* (Super-Kamiokande Collaboration), Atmospheric neutrino oscillation analysis with external constraints in Super-Kamiokande I-IV, Phys. Rev. D **97**, 072001 (2018).
[83] P. A. Zyla *et al.* (Particle Data Group), Review of particle physics, Prog. Theor. Exp. Phys. **2020**, 083C01 (2020).
[84] K Abe, Y Haga, Y Hayato, M Ikeda, K Iyogi, J Kameda, Y Kishimoto, Ll Marti, M Miura, S Moriyama *et al.*, Solar neutrino measurements in Super-Kamiokande-iv, Phys. Rev. D **94**, 052010 (2016).

[85] John F. Beacom and Mark R. Vagins, GADZOOKS! Anti-Neutrino Spectroscopy with Large Water Cherenkov Detectors, Phys. Rev. Lett. **93**, 171101 (2004).
[86] K. Abe *et al.* (Super-Kamiokande Collaboration), Diffuse supernova neutrino background search at Super-Kamiokande, Phys. Rev. D **104**, 122002 (2021).
[87] R. Acciarri *et al.* (ArgoNeuT Collaboration), Demonstration of MeV-scale physics in liquid argon time projection chambers using ArgoNeuT, Phys. Rev. D **99**, 012002 (2019).
[88] Babak Abi *et al.* (DUNE Collaboration), Deep underground neutrino experiment (DUNE), far detector technical design report, Volume I introduction to DUNE, J. Instrum. **15**, T08008 (2020).
[89] Alexander Friedland and Shirley Weishi Li, Understanding the energy resolution of liquid argon neutrino detectors, Phys. Rev. D **99**, 036009 (2019).
[90] Fengpeng An *et al.* (JUNO Collaboration), Neutrino physics with JUNO, J. Phys. G **43**, 030401 (2016).
[91] Kevin J. Kelly, Pedro A. N. Machado, Ivan Martinez-Soler, Stephen J. Parke, and Yuber F. Perez-Gonzalez, Sub-GeV Atmospheric Neutrinos and *CP* Violation in Dune, Phys. Rev. Lett. **123**, 081801 (2019).
[92] A. M. Dziewonski and D. L. Anderson, Preliminary reference Earth model, Phys. Earth Planet. Interiors **25**, 297 (1981).
[93] W. F. McDonough, 3.16—compositional model for the Earth's core, in *Treatise on Geochemistry (Second Edition)*, edited by Heinrich D. Holland and Karl K. Turekian (Elsevier, Oxford, 2014), pp. 559–577.
[94] Frederick K. Lutgens, Edward J. Tarbuck, and Dennis G. Tasa, *Essentials of Geology* (Pearson Higher Ed, Hoboken, NJ, 2011).
[95] Kaushik Borah, Richard J. Hill, Gabriel Lee, and Oleksandr Tomalak, Parametrization and applications of the low-Q^2 nucleon vector form factors, Phys. Rev. D **102**, 074012 (2020).
[96] J. Arrington, Implications of the discrepancy between proton form factor measurements, Phys. Rev. C **69**, 022201 (2004).
[97] J. A. Formaggio and G. P. Zeller, From eV to EeV: Neutrino cross sections across energy scales, Rev. Mod. Phys. **84**, 1307 (2012).
[98] C. H. Llewellyn Smith, Neutrino reactions at accelerator energies, Phys. Rep. **3**, 261 (1972).
[99] Tie-Jiun Hou *et al.*, New CTEQ global analysis of quantum chromodynamics with high-precision data from the LHC, Phys. Rev. D **103**, 014013 (2021).
[100] André de Gouvêa, Patrick J. Fox, Boris J. Kayser, and Kevin J. Kelly, Three-body decays of heavy Dirac and Majorana fermions, Phys. Rev. D **104**, 015038 (2021).